Ore Geology Reviews 155 (2023) 105361

Contents lists available at ScienceDirect

Ore Geology Reviews

journal homepage: www.elsevier.com/locate/oregeorev

The Peña do Seo W-Sn deposit, NW Iberia: Petrology, fluid inclusions and O-H-S isotopes

P. Caldevilla [a,*], L. González-Menéndez [b], T. Martín-Crespo [c], E. Vindel [d], A. Guedes [e], E. Berrezueta [f], A.M. Castañón [a], F. Gómez-Fernández [a]

[a] Dpto. Tecnología Minera, Topografía y Estructuras, E.S.T.I. de Minas, Universidad de León, Avda. Campus de Vegazana s/n, 24007 León, Spain
[b] Instituto Geológico y Minero de España (IGME-CSIC), Av. Real 1, Parque Científico, 24006 León, Spain
[c] Dpto. Biología y Geología, Universidad Rey Juan Carlos, 28933, Móstoles, Madrid, Spain
[d] Dpto. Mineralogía y Petrología, Facultad de Ciencias Geológicas, Universidad Complutense de Madrid, 28040 Madrid, Spain
[e] Dpto. Geociências, Ambiente e Ordenamento do Território – Instituto de Ciências da Terra (ICT), Pólo-Porto, Faculdade de Ciências, Universidade do Porto, Rua do Campo Alegre 687, 4169-007 Porto, Portugal
[f] Instituto Geológico y Minero de España (IGME-CSIC), Calle Matemático Pedrayes, 25, 33005 Oviedo, Spain

ARTICLE INFO

Keywords:
W-Sn
Fluid inclusions
Stable isotopes
Granites
Petrology

ABSTRACT

The Peña do Seo W-Sn ore deposit in NW Iberia consists mainly of quartz veins hosted in schists. Vein mineralogy comprises wolframite, cassiterite and minor molybdenite. Peraluminous S-type granites and minor metaluminous granitoid breccias crop out in the same location. Whole rock geochemistry, mineral characterization, fluid inclusions and stable isotope geochemistry have been combined to infer hydrothermal mineralization conditions.

A pre-ore stage (0) involving the alteration of host rocks, three stages of mineralization (I, II and III), and a supergene stage (IV) have been identified. Stage I (oxide-halide-sulfide stage) consisted of a cassiterite-pyrite-fluorite mineralization in granitoid breccias. Stage II (main oxide stage) involved wolframite-rich selvages and wolframite-cassiterite-(molybdenite) quartz veins. Stage III (main sulfide stage) consisted of a sulfide mineralization in quartz veins comprising pyrite and minor arsenopyrite and chalcopyrite.

Three types of fluid inclusions were found in vein quartz: (1) aqueous two-phase inclusions, with homogenization temperatures (Th) between 445 °C and 280 °C and moderate salinities (9–14 wt% NaCl eq.), (2) aqueous-carbonic three-phase fluid inclusions, with Th from 340 °C to 260 °C and low salinities (2–7 wt% NaCl eq.), and (3) aqueous two-phase fluid inclusions, with Th from 270 °C to 155 °C and low salinities (0–6 wt% NaCl eq.). $\delta^{18}O$ values in quartz from mineralized veins range from +11.2‰ to +13.4‰, and between +15.0‰ and +15.4% in quartz from mineralized granitoid breccias. $\delta^{34}S$ values in sulfides (pyrite, arsenopyrite and chalcopyrite) range between +13.0 ‰ and +37.1 ‰, thus suggesting a marine source of sulfate and possible equilibration with host-rock sulfides. δD values in muscovite and chlorite from quartz veins range between −105.7 ‰ and −71.5 ‰ and between −69.4 ‰ and −67.1 ‰, respectively, indicating a transition from magmatic to magmatic-metamorphic conditions.

An aqueous (H_2O–NaCl) magmatic-hydrothermal fluid led to the W-Sn mineralization, as deduced from the studied fluid inclusions and isotopic signatures. High W and Sn contents in the peraluminous granites indicate that the W-Sn mineralization in Peña do Seo could partially be related to the granites and granitoid breccias. Whereas the Sn (±W) likely derived from hydrothermal fluids exsolving from the crystallizing magmas, host quartz schists would have supplied other elements required for wolframite deposition such as Fe and Mn. Sulfide mineralization in stage III was probably driven by fluid dilution.

* Corresponding author.
E-mail addresses: pcald@unileon.es (P. Caldevilla), l.gonzalez@igme.es (L. González-Menéndez), tomas.martin@urjc.es (T. Martín-Crespo), evindel@ucm.es (E. Vindel), aguedes@fc.up.pt (A. Guedes), e.berrezueta@igme.es (E. Berrezueta), amcasg@unileon.es (A.M. Castañón), fgomf@unileon.es (F. Gómez-Fernández).

https://doi.org/10.1016/j.oregeorev.2023.105361
Received 15 March 2022; Received in revised form 10 February 2023; Accepted 20 February 2023
Available online 25 February 2023

1. Introduction

Tin and tungsten are strategic metals of great importance for industrial and technical uses. Tungsten has been considered as a Critical Raw Material by the European Union due to its strong economic importance and risk of supply and therefore research on tungsten deposits is now a priority in Europe (European Commission, 2010, 2011, 2020a, 2020b). Tin has been recently included in the list of strategic minerals by China (The State Council of the People's Republic of China, 2016) and in the list of critical materials by the United States (Department of the Interior, 2018). Its global supply has been in deficit since 2018 (European Commission, 2020c).

Understanding how Sn and W were able to reach economic concentrations has always been the target of ore deposit research. Common questions regarding Sn-W deposits relate to the sources from where these elements were derived, the nature of the fluids that transported them and the processes and conditions that led to the precipitation and ore formation (e.g., Audétat et al., 1998; Lehmann, 2021). Its frequent spatial association with granite intrusions suggests a direct relationship in which the differentiation of granite magmas enriches residual melts in these elements; exsolved magmatic fluids can subsequently lead to economic concentrations (Hannah and Stein, 1990). The role of magmatic-hydrothermal fluids in the precipitation of W and Sn has been highly debated. Mixing of magmatic and meteoric fluids (Audétat et al., 1998; Heinrich, 2007; Wei et al., 2012; Legros et al., 2019; Harlaux et al., 2021a, 2021b), fluid-rock interaction (Lecumberri-Sánchez et al., 2017b), depressurization and boiling (Korges et al., 2017) and hydraulic fracturing (Liu et al., 2018) have been proposed to be the main processes triggering mineralization.

In this research we study the Peña do Seo W-Sn deposit located in NW Spain. The Peña do Seo deposit is located in the so called "Iberian Sn-W Metallogenic Province" (Cotelo-Neiva, 1944), which is part of the European Variscan Belt of Western Europe. This Belt comprises the northwest and central/western Iberia (Mangas and Arribas, 1988a, 1988b; Noronha et al., 1992; Vindel et al., 1995; Llorens, 2011; Llorens and Moro, 2012a, 2012b; Moura et al., 2014; Chicharro et al., 2015, 2016; Lima et al., 2019), Cornwall in the southwest of UK (Jackson et al., 1982, 1989), the French Central Massif (Marignac and Cuney, 1999; Vallance et al., 2001; Harlaux et al., 2018a, 2018b, 2021a; Monnier et al., 2019) and the Bohemian Massif (Štemprok, 1967; Seltmann and Štemprok, 1994; Korges et al., 2017) among other provinces. Apart from Peña do Seo, there are other important W-Sn ore deposits in the NW of Spain, such as Virgen de la Encina (Arribas, 1982) and Montearenas (Deicha, 1973), to the east, and Casaio (Ourense) and the Calabor district (Zamora), to the south (Burkhardt and García, 1985; Junta de Castilla y León, 1986; Fernández-Fernández et al., 2019).

In the Iberian Peninsula, these W-(Sn) deposits are commonly genetically related to the intrusion of syn- to post-tectonic Variscan peraluminous granites (Noronha, 2017). Tin-tungsten deposits in Iberia include skarn such as Los Santos (Tornos and Casquet, 1984; Tornos et al., 2001, Timón-Sánchez et al., 2009) and Morille (Pellitero, 1981a, 1981b; Timón-Sánchez et al., 2018), pegmatites and leucogranite cupolas, such as Enaras (Arribas, 1982b) and Golpejas (Gonzalo and García, 1984), quartz veins, as Panasqueira (Kelly and Rye, 1979; Polya, 1988, 1989; Noronha et al., 1992; Lecumberri-Sánchez et al., 2017a), Barruecopardo (Pellitero, 1981a) and Peña do Seo (Kronsell, 2019; Bergström, 2020; this work), or combined greisen-quartz vein type, as Logrosán (Chicharro, 2010; Chicharro et al., 2015, 2016). In the case of Borralha, a breccia pipe has been also identified (Noronha, 1983; Gonçalves et al., 2017).

The present work aims to provide the first systematic field relationships and mineralogy description of the Peña do Seo W-Sn vein-type ore deposit. This deposit is hosted in quartz veins crosscutting Neoproterozoic schists spatially related to peraluminous and metaluminous Variscan granitoids. The field relations among these rocks and optimal outcrop conditions make this deposit suitable to investigate the genesis of granite-related W-Sn deposits. Ore-forming conditions have been constrained through the study of the mineral paragenesis, fluid inclusions and O-H-S stable isotope data.

2. Regional geology

2.1. Geological setting

According to the division of the Iberian Variscan Massif (IVM) proposed by Pérez-Estaún et al. (2004), the Peña do Seo area belongs to the Western Asturian-Leonese Zone (WALZ), formed by Cambro-Ordovician (±Neoproterozoic) sedimentary sequences. These rocks were deformed during the Iberian Variscan Orogeny (ca. 370–290 Ma, Martínez-Catalán et al., 2009). In this context of deformation, the Seo-Arnadelo Anticline developed.

The sedimentary record in the study area spans from the Neoproterozoic to the Middle Cambrian. The Neoproterozoic strata are represented by the Serie de Villalba Formation, a sequence of tourmalinized muscovite quartz-schists and grey/black slates. The Lower Cambrian (Cándana, Capas de Transición and Vegadeo Formations) consists of slates/schists, quartz-schists/sandstones, quartzites ± microconglomerates, and carbonate and calc-silicate layers (Matte, 1968; Zamarreño, 1975; Abril Hurtado et al., 1981 and references therein). Neoproterozoic schists are exposed along the axial zone of the Seo-Arnadelo Anticline (Villalba/Narcea Formation; Martínez-Catalán et al., 1990, 2007) and are the host rock of the studied mineralized veins (Figs. 1, 2A–B).

Close to the studied W-Sn deposits, the Cadafresnas granites crop out. They form small stocks belonging to the Boal-Los Ancares magmatic belt and have been dated at 289 ± 3 Ma through U-Pb in zircon (Suárez, 1970; Fernández-Suárez, 1994; Fernández-Suárez et al., 2000). These granite stocks consist of: i) granites (leucogranites ± monzogranites and aplite dikes) and ii) granitoid breccias.

Neoproterozoic schists in the study area record both regional and contact metamorphism. Low-grade regional metamorphism is common in the WALZ, being more intense towards the west (Fernández-Suárez, 1994; Martínez et al., 2004). Regional metamorphism is *syn*-kinematic to the main deformational phases, and reached the greenschist facies, within the chlorite/biotite zone (Fernández-Suárez et al., 2000; Rodríguez Fernández et al., 2021).

2.2. Field observations and geological background

At a local scale, contact metamorphism can be observed in two areas: i) close to the Cadafresnas granite, where it produced a small metamorphic aureole with a "spotty" texture in the host quartz schists (Suárez, 1970); and ii) in the mine area, where a concealed granitoid generated heat, dehydration and silicification of the host rock and developed biotite porphyroblasts cutting the schistosity (Chl + Ms → Bt + And + Qz + fluid-H_2O; Fernández-Suárez, 1994).

The granites cropping out in the area (Cadafresnas granites and granitoid breccias) are late/post-tectonic, in relation to the main Variscan deformation phases, and spatially related to the observed mineralization (Figs. 2C–D) that occurs in adjacent Neoproterozoic schists (Figs. 1, 2A–B). These granites (Fig. 2E–F) are part of a N-S belt of S-type peraluminous ± I-type metaluminous granitoids emplaced at pressures ≤2 kbar (Boal-Los Ancares belt; Suárez, 1970; Fernández-Suárez, 1994; Corretgé et al. 2004). Aplite-porphyry dikes, which were only found inside mine galleries, crosscut the host quartz schists and are 30–50 cm wide (Fig. 2G).

The Neoproterozoic schists hosting the mineralization are mainly composed of quartz, muscovite and chlorite, as well as sericite, K-feldspar, epidote, magnetite, pyrite, chalcopyrite and covellite as accessory minerals. Pyrite is interpreted to be pre-kinematic, since it combs the matrix foliation, generates pressure shadows and does not feature oriented inclusions of minerals. The mineralization, mainly wolframite and

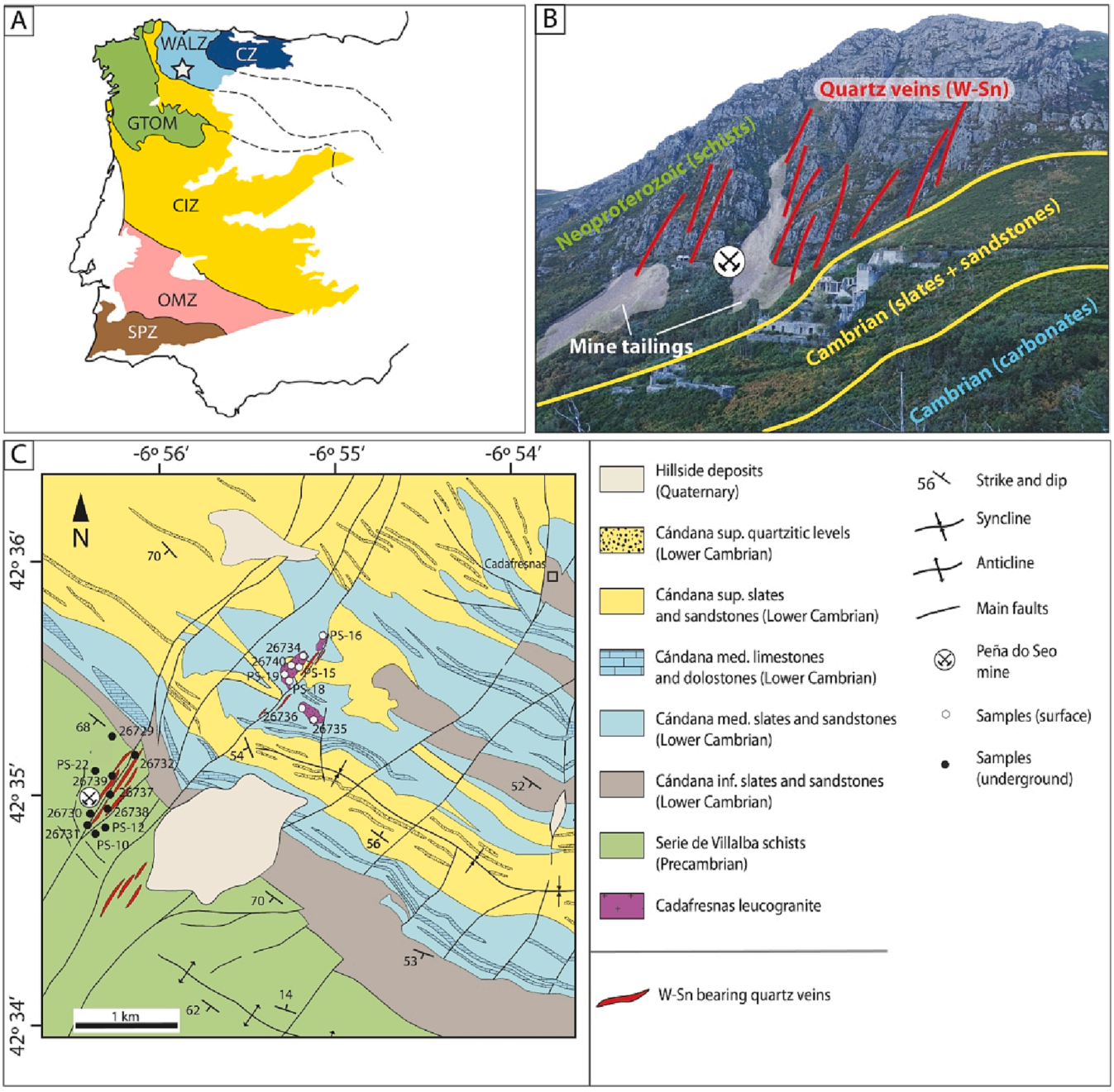

Fig. 1. A) Map of the different zones of the Iberian Variscan Massif, based on Julivert et al. (1972). WALZ: West Asturian-Leonese Zone; CZ: Cantabrian Zone; GTOM: Galicia-Trás-Os-Montes Zone; CIZ: Central-Iberian Zone; OMZ: Ossa Morena Zone; SPZ: South Portuguese Zone. The location of Peña do Seo mine is marked with a star, within the WALZ. B) General view of the deposit, facing west. C) Geological map of the area of study, modified after Abril-Hurtado et al. (1981).

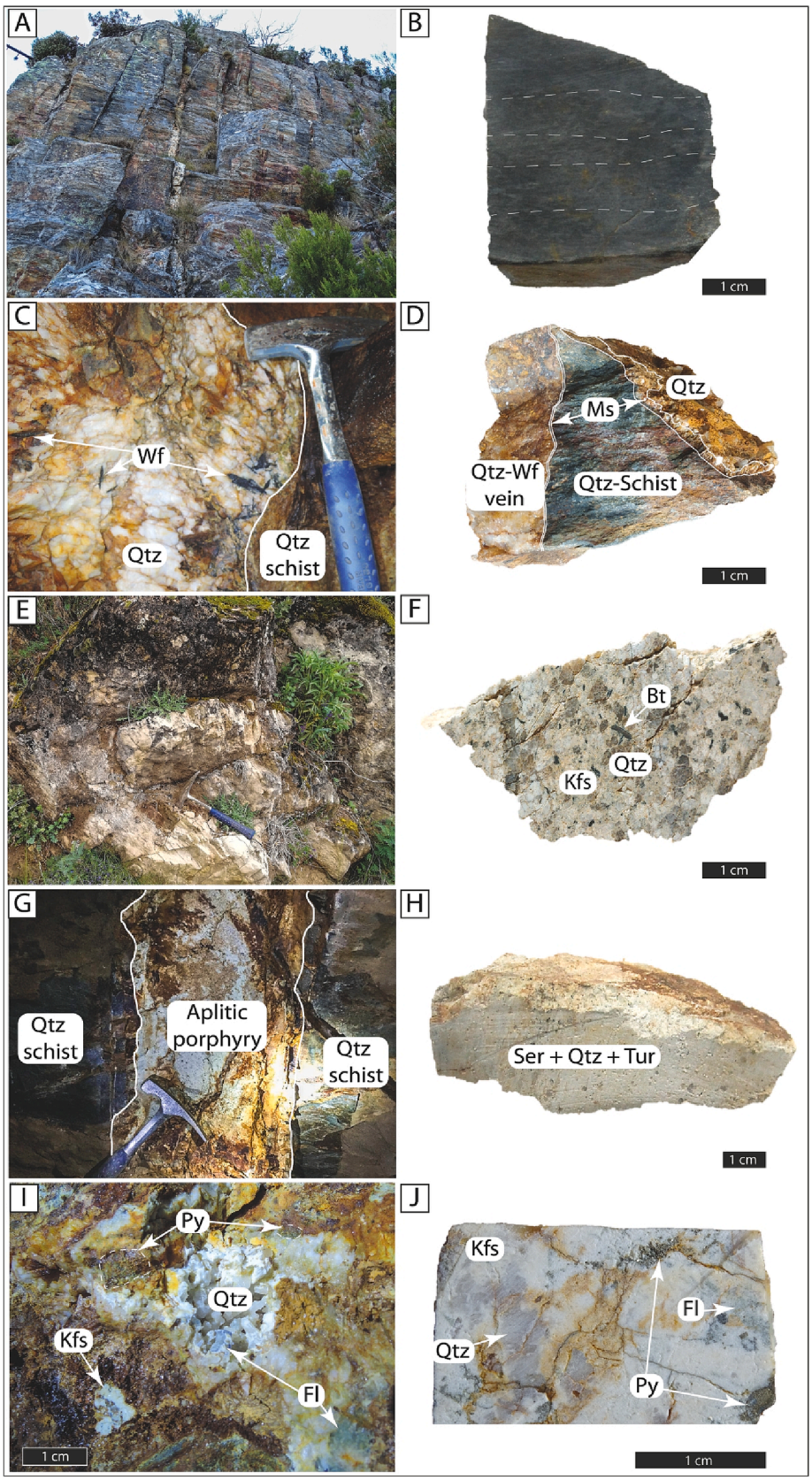

Fig. 2. Field and and hand sample images, respectively, of the host quartz schists (A, B), the W-Sn bearing quartz veins (C, D), the leucogranite (E, F), the aplite (G, H) and the granitoid breccia (I, J). White dashed lines in B) indicate schistosity. Wf: wolframite; Qtz: quartz; Ms: muscovite; Kfs: K-feldspar; Bt: biotite; Ser: sericite; Tur: tourmaline; Py: pyrite; Fl: fluorite.

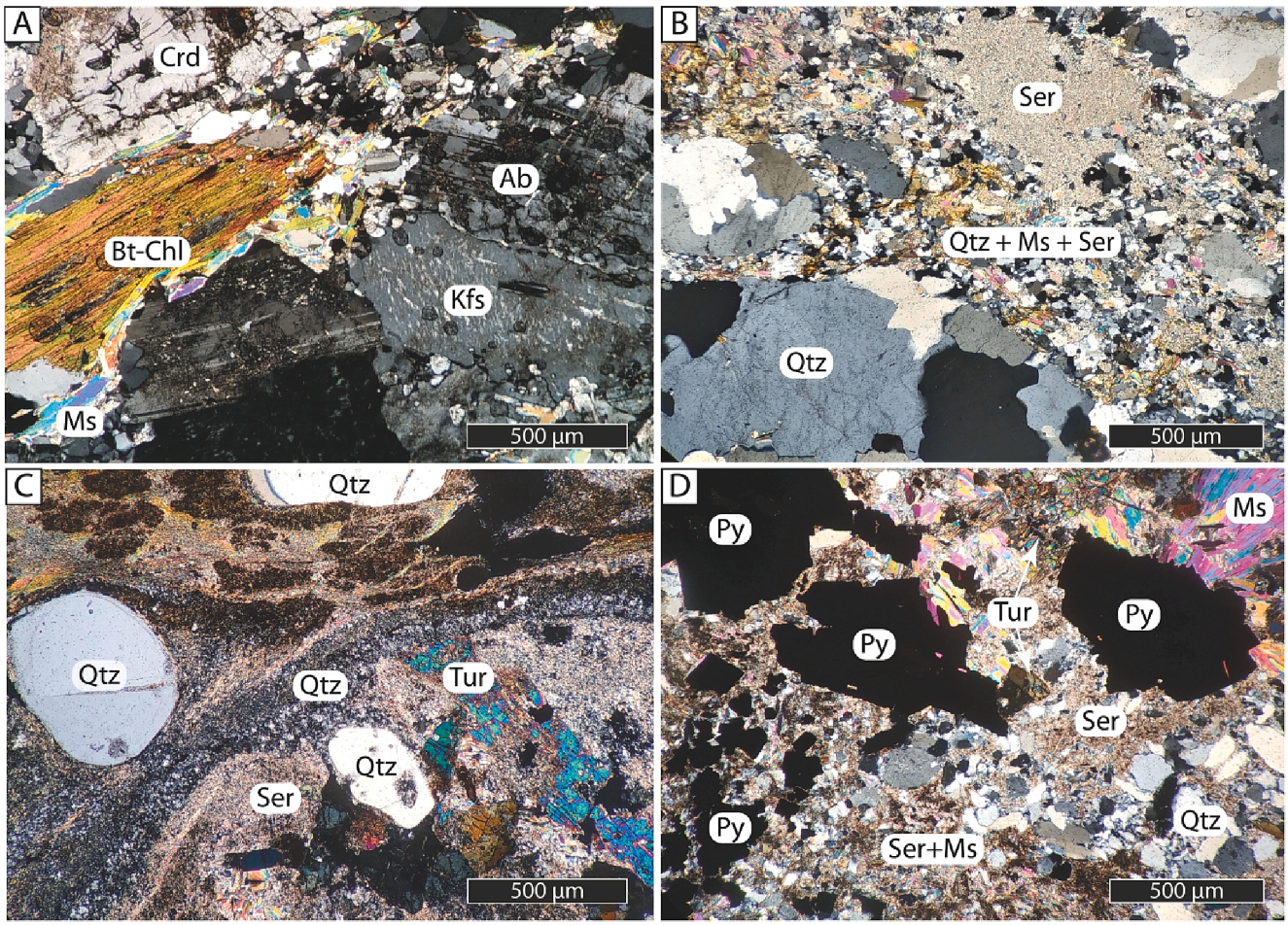

Fig. 3. Representative photographs and microphotographs of main igneous rocks in Peña do Seo. A,: leucogranite showing signs of alteration, with secondary sericite replacing K-feldspar and albite, and cordierite partially pinitized. B: altered granite. C: aplitic porphyry. D: Granitoid breccia. Ab: Albite; Bt: biotite; Chl: chlorite; Crd: cordierite; Kfs: K-feldspar; Ms: muscovite; Py: pyrite; Qtz: quartz; Ser: sericite; Tur: tourmaline. All pictures with crossed nicols.

much less abundant cassiterite, appears in subvertical quartz veins striking NNE-NE (N40E on average; Fig. 1), although considerable cassiterite mineralization is also found in granitoid breccias as well.

3. Materials and methods

3.1. Field work and sampling

Eighteen representative samples from the Variscan granitic rocks, Neoproterozoic country rock schists and mineralized quartz veins were collected (Figs. 1-2, Table 1). Eight of the samples were taken in outcrops surrounding the mine and in the dump. The other ten samples were taken in different underground adits (Fig. 1, Table 1). Thin sections, polished thin sections and polished slabs were prepared for microscopy analysis.

3.2. Microscopy and cathodoluminescence

Thin sections of the Variscan granitic rocks, Neoproterozoic country rock schists and mineralized quartz veins (I and II) were prepared and then studied under a Nikon Eclipse E600 microscope at the School of Mines in the University of León with both transmitted and reflected light. A JEOL 6100 LV Scanning Electron Microscope (SEM) equipped with an Energy-Dispersive Spectrometer (EDS) at the Microscopy Service Facilities in the University of León was also used for determining the mineral phases, as well as for taking microphotographs of the samples. Analyses were performed using a working distance of 10 mm, accelerating voltage of 20 kV, spot size of 50 µm and current of 15nA. Cathodoluminescence (CL) imaging was performed using a CITL Mk5 cold cathode operating at 15 kV and 400 mA at the CIUDEN laboratories in Cubillos del Sil, León, Spain.

3.3. Whole-rock geochemistry

Eighteen representative samples of the Variscan granitic rocks, Neoproterozoic host country rock schists and mineralized quartz veins were analyzed for whole-rock geochemistry. Rocks were sent for analysis to the ALS laboratories in Ireland. Rock analyses were performed by ICP-AES (Inductively Coupled Atomic Emission Spectroscopy) for major elements and ICP-MS (Inductively Coupled Mass Spectrometer) for trace and rare earth elements using the ME-ICP06 and ME-MS81 packages (https://www.alsglobal.com). In ME-ICP06, a prepared sample (0.100 g) was added to lithium metaborate/lithium tetraborate flux, mixed well and fused in a furnace at 1000 °C. The lowest detection limit was 0.01 wt % The resulting melt was then cooled and dissolved in 100 ml of 4 % nitric acid + 2 % hydrochloric acid. This solution was then analyzed by ICP-AES and the results were corrected for spectral inter-element interferences. In MS81, a prepared sample (0.100 g) was added to lithium metaborate/lithium tetraborate flux, mixed well and fused in a furnace at 1025 °C. The resulting melt was then cooled and dissolved in an acid mixture containing nitric, hydrochloric and hydrofluoric acids. This solution was then analyzed by inductively coupled plasma - mass spectrometry. The lowest detection limit for this method ranged between 0.01 and 10 ppm, depending on the analyzed element.

3.4. Fluid inclusion study

Microthermometry studies of around 200 fluid inclusions on eleven samples of quartz were carried out on doubly-polished wafers (250–300 μm in thickness) using a Linkam THMSG600 heating-freezing stage (Shepherd et al., 1985) at the Department of Mineralogy and Petrology of the Faculty of Geology in the Universidad Complutense de Madrid. The calibration curve employed was generated from melting points of solid standards at T > 25 °C, and melting points of H_2O and H_2O–CO_2 of synthetic inclusions at T < 0 °C. The rate of heating was 0.1 °C/min when phase transitions were approached, in order to get an accuracy of ±0.2 °C for final ice melting at T < 0 °C, and of ±4 °C for homogenization temperatures over 25 °C.

The phase volume-fractions were visually estimated. Raman microspectrometry analyses were performed on a Jobin Yvon-Spex XY Raman spectrometer at Earth Sciences Institute, pole of the University of Porto and the quantification of the different volatile species in the inclusions was obtained following methods described by Prieto et al. (2012). Bulk composition and density were computed from P–V–T–X properties of individual fluid inclusions in the C–O–H–System (Dubessy, 1984; Dubessy et al., 1989; Thiéry et al., 1994). Bulk composition and density of representative fluid inclusions were calculated from microthermometric measurements and Raman analyses of the volatile phase using a clathrate stability model (Dubessy et al., 1992; Bakker et al., 1996; Bakker, 1998) and the CLATHRATES package software (Bakker, 1997). Isochores were calculated with the ISOC computer program of the FLUIDS package (Bakker, 2003; Bakker and Brown, 2003) using the equation of state of Bowers and Helgeson (1983) and Bakker (1999) for the volatile-bearing fluid inclusions and the equation of state of Zhang and Frantz (1987) for the aqueous fluid inclusions. Salinity for the H_2O-NaCl system was calculated using the equation of state of Bodnar (1993), whereas salinity for the H_2O-CO_2-CH_4-N_2-NaCl system was calculated from the clathrate melting temperature using the equations of state of Thiéry et al. (1994) and Duan et al. (1996).

3.5. Stable isotopes

Stable isotope analyses were performed at the isotope facilities in the Universidad de Salamanca, Spain. Twenty-nine $^{18}O/^{16}O$ analyses were performed in twelve representative samples of quartz, biotite, muscovite and chlorite. These samples were analyzed through laser fluorination, involving total sample reaction with excess ClF_3 (Borthwick and Harmon, 1982) using a CO_2 laser as a heat source (in excess of 1500 °C; according to Sharp, 1990). Resulting O_2 was then converted to CO_2 by reaction with hot graphite (Clayton and Mayeda, 1963) and analyzed on line by a VG-Isotech SIRA-II mass spectrometer. Reproducibility was better than ± 0.3 ‰ (1σ), based on repeat analyses of internal and external standards during sample runs. Results are given in standard notation ($\delta^{18}O$) as per mil (‰) deviations from the VSMOW standard. Regarding sulfur isotopes, seventeen analyses were performed in five samples of pyrite, arsenopyrite and chalcopyrite by standard techniques (Robinson and Kusakabe, 1975), with SO_2 being liberated by combusting with excess Cu_2O at 1075 °C, in vacuum. Liberated gases were analyzed on a VG Isotech SIRA II mass spectrometer, and standard corrections applied to produce $\delta^{34}S$ values. Standards used were international standards NBS-123 and NBS-127, with 1σ reproducibility better than ± 0.2 ‰. Results are given in $\delta^{34}S$ notation as per mil (‰) deviations from the Vienna Canyon Diablo Troilite (V-CDT) standard. For D/H isotopic analysis, fourteen analyses were performed on six samples of biotite, muscovite and chlorite. Extraction of H_2 and H_2O was performed through the uranium technique, as explained in Godfrey (1962), with updates by Jenkin (1988). Samples were heated up to 1500 °C and H_2O was converted to H_2 by reduction over the depleted uranium. Hydrogen and oxygen isotope ratios were measured in a SIRA-II mass spectrometer. Data is reported relative to V-SMOW.

4. Results

4.1. Petrology of the Variscan granites (Cadafresnas stocks and granitoid breccias)

4.1.1. Field relations and petrography

The Cadafresnas granites are two-mica and, in general, their mineralogy and composition are similar to those of the Ponferrada granite. These granites trend N60E, roughly parallel to the Variscan structures, but in detail they crosscut these structures, being tardi- to post-Variscan. Their mineralogy consists of K-feldspar (Kfs: 35 %), albite (Ab: 25 %), quartz (Qtz: 20 %), muscovite (Ms: 10 %) ± biotite (Bt: 5–10 %) ± garnet (Grt: <2 %) ± pseudomorphically altered cordierite (Crd: <2 %, Fig. 3). The accessory minerals observed are apatite and zircon. The granite intrusion produced a thermal aureole and a spotty texture in the quartz schists defined by biotite + tourmaline (Suárez, 1970). These granites are hydrothermally altered, with albite and sericite as typical replacement phases after K-feldspar and muscovite, respectively, and pinite replacing cordierite (Fig. 3A).

Aplite-porphyry dikes crosscut the host quartz schists (Fig. 2G), showing a brecciated texture and being mainly composed of sericite (Ser: 45%), quartz (Qtz: 35%), tourmaline (Tur: 15%), muscovite (Ms: <5%) and chlorite (Chl: <5%). Their texture is porphyritic-bimodal and show subvolcanic features such as quartz embayments (Fig. 3C).

The granitoid breccias are stocks mostly composed of quartz (Qtz: 20%), K-feldspar (Kfs: 20%), muscovite (Ms: 15%), sericite (Ser: 20%), prehnite (Prh: 5%), fluorite (Fl: <5%) and cassiterite (Cst: < 5%) (Fig. 2J). A Pb-Bi-Ag sulfosalt, waylandite and native bismuth overgrowing disseminated pyrite in the muscovite-sericite matrix appear in minor amounts.

4.1.2. Geochemistry

Since the analyzed granitic samples are variably altered (see section 4.2 below), their modal classification through the QAPF diagram of Streckeisen (1976) will be not attempted and the following statements about their major element composition should be taken with the opportune cautions. All samples are peraluminous, (A/CNK = 1.22–3.78) with low CaO (0.01–0.42 wt%), Na_2O (0.1–3.2 wt%) and P_2O_5 (0.02–0.1 wt%) and relatively elevated K_2O (2.9–4.75 wt%) contents (Table 1, Fig. 4A and 4B). The very high A/CNK values of some samples could be indeed indicative of hydrothermal alterations that removed part of the CaO, Na_2O and possibly P_2O_5. The projection of the major element data in the classification diagram of Villaseca et al. (1998) shows the elevated peraluminous character of these rocks and the positive correlation of the A parameter (equivalent to the A/CNK molar ratio) with the B maficity parameter (FeO_t + MgO + TiO_2 wt.%, Fig. 4), characteristic of S-type granites (Villaseca et al., 1998). On the other hand, these granites also display relatively elevated F contents (260–690 ppm), high FeO_t/MgO (3.3–24.9 wt%), Na_2O + K_2O/CaO and Ga/Al ratios (Table 1), which suggest a very fractionated nature and/or a slight A-type signature (Whalen, et al., 1987). This geochemistry is similar to that of other Variscan late/post-tectonic known as “G3 type” (Capdevila, 1969; Capdevila and Floor, 1970) granites: peraluminous, and low in CaO and P_2O_5 contents (Fernández-Suárez, 1994; Cuesta and Gallastegui, 2004; González-Menéndez et al., 2019).

The chemical composition of granitoid breccias shows different A-B relations compared to the Cadafresnas granites in Fig. 4. Their CaO, FeO_t and TiO_2 contents are higher (Table 1) and have metaluminous A/CNK values (0.66–1.02). K_2O (2.16–3.1 wt%) is lower but Na_2O (0.05–4.41 wt%) is higher on average compared to the Cadafresnas granites. This indicates a different origin for these rocks. Its Na_2O + K_2O/CaO and Ga/Al ratios are closer to standard I/S granitoids but display higher FeO_t/MgO (6.4–12.6 wt%) and F contents (≥2 wt%).

Regarding trace element compositions, the Cadafresnas granites show high Rb contents (139–700 ppm) and moderate to low contents in the other trace elements. Many of the trace elements decrease (Li, Rb,

Table 1
Whole-rock major (wt. %) and trace-element (ppm) compositions of the most relevant rocks in Peña do Seo. Temperatures estimated using zircon saturation temperature (ZST, Watson and Harrison, 1983).

	Cadafresnas stock												Schists		Altered schists			Quartz vein
	Granites									Granitoid breccias								
	Leucogranites				Altered granites				Aplite									
Sample	26734	26740	PS-15	PS-16	26735	26736	PS-18	PS-19	26730	26731	PS-10	PS-12	PS-22	26729	26732	26737	26738	26739
SiO_2	76.6	75.8	74	76.5	74.1	63.6	81.7	86	74.8	71.8	70.7	81.1	60.2	63.2	78.7	28.6	53.8	91.8
Al_2O_3	13.3	14.3	14.45	13.45	14.2	23.2	10.2	7.43	14.9	11.2	11.55	5.71	16.1	17.3	9.4	13.1	22.2	0.4
Fe_2O_3	1.7	1.6	2.21	1.91	2	2.8	1.66	1.66	2.2	5	3.94	4.92	6.76	7.8	5.2	34.1	6.8	4
CaO	0.3	0.2	0.25	0.42	0.3	0.1	0.04	0.01	0.1	2.6	3.64	3.79	3.88	0.4	0.1	0.1	0.1	0.1
MgO	0.1	0.2	0.19	0.09	0.3	0.6	0.06	0.21	0.6	0.7	0.28	0.38	2.06	2.1	0.9	0.6	1.7	0
Na_2O	2.6	3.1	1.63	3.2	1.5	0.1	2.23	0.16	0.2	1.7	4.41	0.05	0.24	0.3	0.2	0.1	0.8	0
K_2O	4.5	4.6	4.75	4.59	5.2	7.4	4	2.9	3.2	3.1	2.16	2.3	3.32	3.9	2	3.3	3.9	0.1
TiO_2	0.05	0.05	0.05	0.02	0.05	0.1	0.03	0.01	0.1	0.3	0.3	0.06	0.83	1	0.4	0.3	1.1	0
MnO	0.1	0	0.06	0.03	0.1	0.1	0.02	0.02	0	0	0.02	0.02	0.08	0.1	0.1	0	0.1	0
P_2O_5	0.1	0	0.04	0.05	0.1	0	0.04	0.02	0.1	0.1	0.03	0.06	2.98	0.2	0.1	0.8	0.1	0.1
LOI	100.3	100.8	100.5	101.1	99.6	101	100.77	100.7	99.8	99.3	99.94	101.51	99.82	99.7	98.8	90.9	93.4	98.5
Total	76.6	75.8	74	76.5	74.1	63.6	81.7	86	74.8	71.8	70.7	81.1	60.2	63.2	78.7	28.6	53.8	91.8
Ag	0.1	0.51	<0.5	<0.5	1.7	23.4	<0.5	<0.5	0.16	5.05	5.7	7.5	<0.5	0.39	2.74	6.9	8.53	64.7
As	4.4	156	11.4	16	18	61.7	9.3	8.5	3.510.00	97.4	41.9	>250	1.6	17.6	1.245.00	8.070.00	>10000	>10000
Ba	35.6	58.9	82.3	69.7	96.9	13.8	111.5	109	105.5	835	1140	381	417	432	209	548	414	6.8
Bi	16,3	2,7	1	0,52	17,6	13,8	1,32	2,52	0,6	16,8	24,4	20,9	0,53	1,8	6,6	64,4	12,7	1,36
Cd	0,0001	0,11	0,01	0,01	0,1	0,09	0,01	0,01	0,04	4,29	2,2	8,4	6	5,21	1,17	47,6	3,4	380
Ce	21.8	15.65	39	27.4	25.6	32.1	20.1	13.6	36.6	34.6	28.7	24.1	6	85.3	40.2	99.6	61.9	1.4
Cl	–	–	<50	<50	–	–	160	310	–		60	50	119.5					
Co	0.7	0.4	1	<1	0.6	1.1	<1	<1	1.5	6.6	8	2	13	14.1	3.1	2.5	7.7	0.5
Cr	11	11	20	20	9	7	170	30	10	41	50	40	170	103	61	100	36	29
Cs	9.5	9.87	9.63	9.29	7.98	24.1	5.71	3.05	63.6	24.9	7.31	10.8	34.5	45.3	61.9	80.1	82.5	1.42
Cu	21	169	74	2	253	44	17	13	16	241	23	1310	25	77	136	78	1.140	1.395
Dy	4.3	5.5	7.27	7.03	4.6	8.5	4.62	3.15	5.8	3.7	3.8	3.92	16.55	6	3.8	5.3	5.4	<0.05
Er	1.9	1.7	3.83	2.59	2.4	4.4	2.52	1.25	2.9	2.2	2.22	2.43	7.73	3.6	2.1	3.1	2.4	0.1
Eu	0.1	0.1	0.12	0.14	0.1	0.2	0.15	0.06	0.5	0.7	0.56	0.55	3.26	1.5	0.8	1.6	1.9	0
F	–	–	690	440	–	–	350	260	–	–	>20000	>20000	–	–	–	–	–	–
Ga	22.9	29.6	21.9	21.1	23.6	40.6	14.8	9.2	20	12.6	6.5	4.1	23.7	24.3	15.2	31.3	14.4	2.4
Gd	3.7	6	6.27	6.44	3.1	5.9	6.27	6.44	5	3.5	3.41	3.28	23.3	7.2	3.2	6.6	8	0.1
Hf	2.8	2.1	3	2.4	2.4	0.1	2	1	3.8	5.2	5.4	0.5	8.1	8.4	4.3	7.3	1.7	0.2
Ho	0.7	0.9	1.29	1.05	0.9	3.2	0.88	0.48	1	0.8	0.82	0.83	3.05	1.2	0.7	1.1	1	0
La	10	8.2	15.1	12.2	10.9	12.9	13.4	14.9	16.5	15.4	1.15	0.52	54.6	41.4	18.2	34	24.1	0.8
Li	39.2	12.4	40	60	36.1	95.1	10	10	134	89.3	15	10	140	165	315	383	124	21.1
Lu	0.3	0.2	0.47	0.22	0.3	0.6	0.28	0.3	0.4	0.3	39	15	0.84	0.5	0.3	0.5	0.3	<0.01
Mn	497	230	–	–	484	738	–	–	124	281	–	–	561	503	443	364	310	124
Mo	0.8	0.6	<1	1	6.3	1.5	<1	2	1.5	95.5	2	32	<1	0.8	5.6	1	21.8	36.8
Nb	23.5	23.4	13.7	15.6	14.8	18	9.5	7.8	17.9	17.6	20.7	4.7	14.4	17.9	27.5	18.6	4.1	9.6
Nd	9.8	11.6	16.8	13.2	10	17.9	10.7	7	16.3	14.5	13	9.9	63	39.3	17.6	45.8	34.1	0.7
Pb	16.3	15.7	33	29	15.4	4.5	12	9	19.2	6.9	8	6	22	18.9	4.9	34.2	56.7	749
Pr	2.8	3	4.55	3.64	2.8	5.1	2.98	2.09	4.6	3.8	3.08	2.68	14.85	10.2	4.7	11.8	7.9	0.1
Rb	417	367	265	277	391	700	200	139	389	259	121	133.5	263	382	304	394	412	6
Sb	0.2	0.9	0.14	0.09	1.1	1.1	0.15	0.2	2.5	2	0.84	1.81	0.12	0.5	2.4	5.3	65.4	74.7
Sc	4.1	5.3	5	5	5.5	8.2	3	2	6.4	3.8	2	1	16	18.7	7	20.1	6.1	0.4
Sn	16.9	35.1	18	9	79.1	300	27	4	32.8	96.7	128	2320	19	41	1045	1420	323	2740
Sr	13.3	25.8	13	14	30.3	5.8	59	21.4	39	3	464	45.5	164	82	34.8	153.5	223	8.3
Ta	7.7	4.3	2	1.5	2.9	3.9	1.2	1	69.9	2.4	3.6	0.9	0.8	1.3	5.3	1.2	0.3	0.8
Th	8.3	9.5	12.75	10.75	8	13.7	7.56	4.62	0.9	186.5	4.09	1.25	13.5	14.2	6.3	14.3	4.8	0.2
U	6.3	9.3	5.96	5.06	8.1	6.3	7.33	4.44	7.3	1.8	1.15	0.52	3.91	3.7	2.5	5.5	4.1	0.2
V	2	1	6	7	5	12	0.1	5	9	22	15	10	116	134	64	53	161	7
W	9.8	10.6	5	4	306	18	2	2	26.2	19.5	39	15	36	38	164	2760	356	488
Y	11.3	18.9	38.5	33.5	12.1	16.7	25.6	17.5	23.1	11.9	22.6	27.4	83.2	31.6	19.2	21.7	27.9	0.5
Yb	2.3	1.2	3.75	1.69	2.6	4.5	2.3	0.87	2.7	1.9	2.07	2.23	5.99	3.5	1.9	2.4	3.1	0.1
Zn	37	59	37	47	143	85	12	12	20	114	48	110	138	143	92	319	151	20
Zr	31.1	28.8	52	40	33.9	50.7	45	12	67.4	59.6	197	19	295	292	144	58	252	0.1
ZST (°C)	683.8	676.9	735.3	693.4	699.5	747.3	709.9	645.7	787.8	709.3	756.8	595.7						

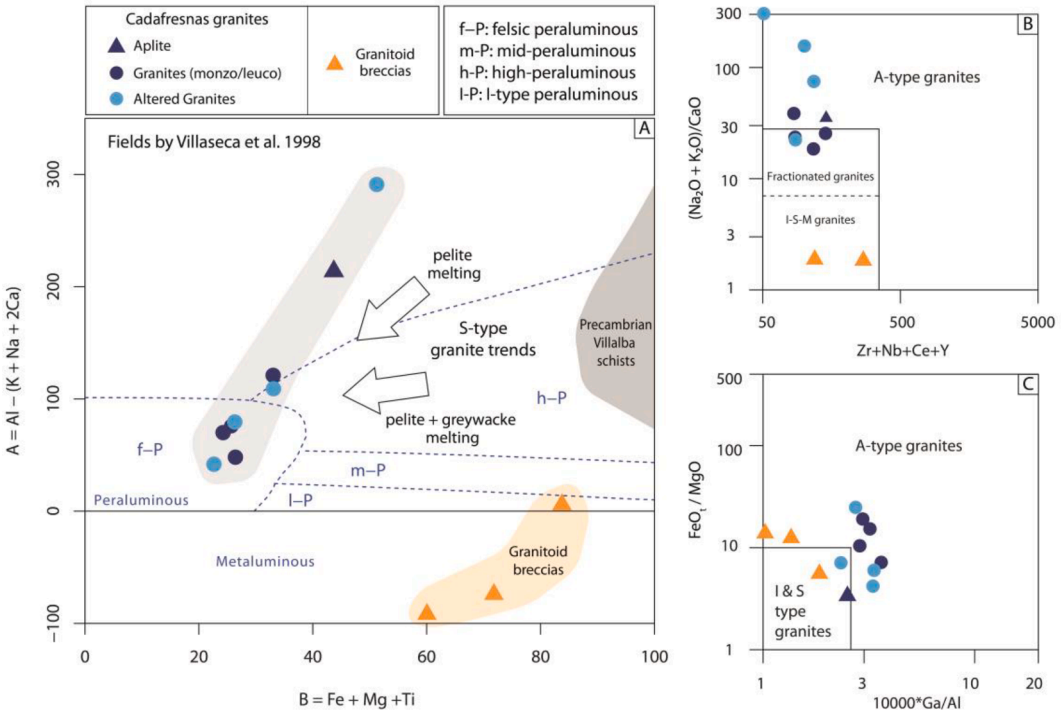

Fig. 4. A) Classification diagram for igneous rocks modified by Villaseca et al. (1998). The samples from the Neoproterozoic schists (Villalba/Narcea Formation) were plotted in the diagram. B) and C) Classification diagram for igneous rocks of Whalen et al. (1987), designed to discriminate between A-type granitoids and I-S-M granitoids.

Th, Nb, Th, V, Sc, Zr, REE, Ga) with increasing SiO_2 and with decreasing maficity ($FeO_t + MgO + TiO_2$; Fig. 5). Most of these elements are carried in biotite and accessory zircon + monazite (Bea 1996; Brown and Korhonen, 2009; Clarke et al., 2021; Michaud et al., 2021). Therefore, a biotite fractionation process could explain these trends. Other trace elements (Pb, U, Ba, Sr) show no significant correlations in binary diagrams with SiO_2. These elements are commonly carried by feldspars (K-feldspar/plagioclase). A more pervasive hydrothermal alteration of these phases could explain the scatter and absence of correlation between these elements and SiO_2. Compared to the Cadafresnas granites, the granitoid breccias have higher Ba (381–1140 ppm) and Sr (45–1140 ppm) contents (Table 1).

C1 chondrite-normalized REE patterns (Fig. 6) have been produced for i) the least altered Cadafresnas granite samples, ii) altered Cadafresnas granites and iii) granitoid breccias. The least altered granites (Fig. 6A) have moderate to low total REE contents (60.45–105.64 ppm, average 82.35 ppm), low fractionated pattern (La_n/Yb_n = 2.74–4.91; avg = 3.82) and high negative Eu anomaly (Eu* =0.06–0.31; avg = 0.12). The altered granites (Fig. 6B) also have moderate to low REE contents (41.63–101.70 ppm, average 68.8 ppm), are slightly less fractionated (La_n/Yb_n = 1.95–5.87; avg = 3.44) and show a more pronounced negative Eu anomaly (Eu* = 0.08–0.12; avg = 0.098). The granitoid breccias (Fig. 6C) show moderate REE contents (68.44–86.10 ppm, average = 76.51 ppm), a slightly more fractionated pattern (La_n/Yb_n = 4.41–5.52; avg = 4.83) and a much less pronounced negative Eu_n anomaly (Eu* = 0.56–0.66; avg = 0.61) than the granite samples.

In the granites, the contents of Sn (58 ppm) and W (43.6 ppm) are elevated (Table 1). These elements show broad positive correlations with $FeO_t + MgO + TiO_2$ and negative correlation with SiO_2, indicating a decrease of W and Sn contents with magmatic differentiation driven by biotite fractionation (Fig. 7, Table 1). In the granitoid breccias, the Sn (848 ppm; 96–2320 ppm) and W (24.5 ppm; 15–39 ppm) contents are higher and similar, respectively, compared to the granites. A broad increase of Sn and W with decreasing maficity ($FeO_t + MgO + TiO_2$) in the granitoid breccias can be observed (Fig. 7). As expected, the quartz vein shows the highest Sn (2740 ppm) and W (488 ppm) contents.

The Nb/Ta and Zr/Hf ratios have been used as markers of magmatic-hydrothermal transition and also as metallogenic markers for peraluminous granites (Ballouard et al., 2016). Those granites with significant fluid interaction usually have K/Rb < 150 and Nb/Ta < 5. In our study, the granites show low K/Rb (68–173, avg <150) and Nb/Ta (2.9–10, avg. > 5). Therefore, most of them are classified as barren. The granitoid breccias, having similar Nb/Ta ratios and K/Rb < 150 would also classify as barren.

4.2. *Hydrothermal alterations in the Cadafresnas Variscan granites and Neoproterozoic schists*

Different types of hydrothermal alteration related to anomalously high W and Sn concentrations have been found in the deposit, both in the granite and in the host quartz schists. The intrusion of these igneous rocks produced a metamorphic halo in the host schist, with abundant tourmaline. Subsequently the hydrothermal alteration occurred:

- Greisenization appears in the easternmost part of the Cadafresnas leucogranites, with feldspars and biotite crystals replaced by muscovite. In other areas the granites show a strong fracturing and a pervasive silicification as a result of the circulation of high temperature fluids.
- Hydrothermal alteration has also transformed the primary plagioclase into K-feldspar (Witt, 1987). This alteration seems to be fracture-controlled, appearing on both sides of the faults and fractures. Quartz is less abundant compared to the unaltered granite.
- Phyllic alteration affects the host rocks, i.e., Neoproterozoic micaschists, with primary muscovite and chlorite being altered to a mass of sericite and muscovite. Where this alteration is more intense, close to the quartz veins, smectite, montmorillonite and kaolinite occur.
- Tourmalinization: it affects the quartz schists in their proximity to the quartz veins. Tourmaline partially replaces muscovite.

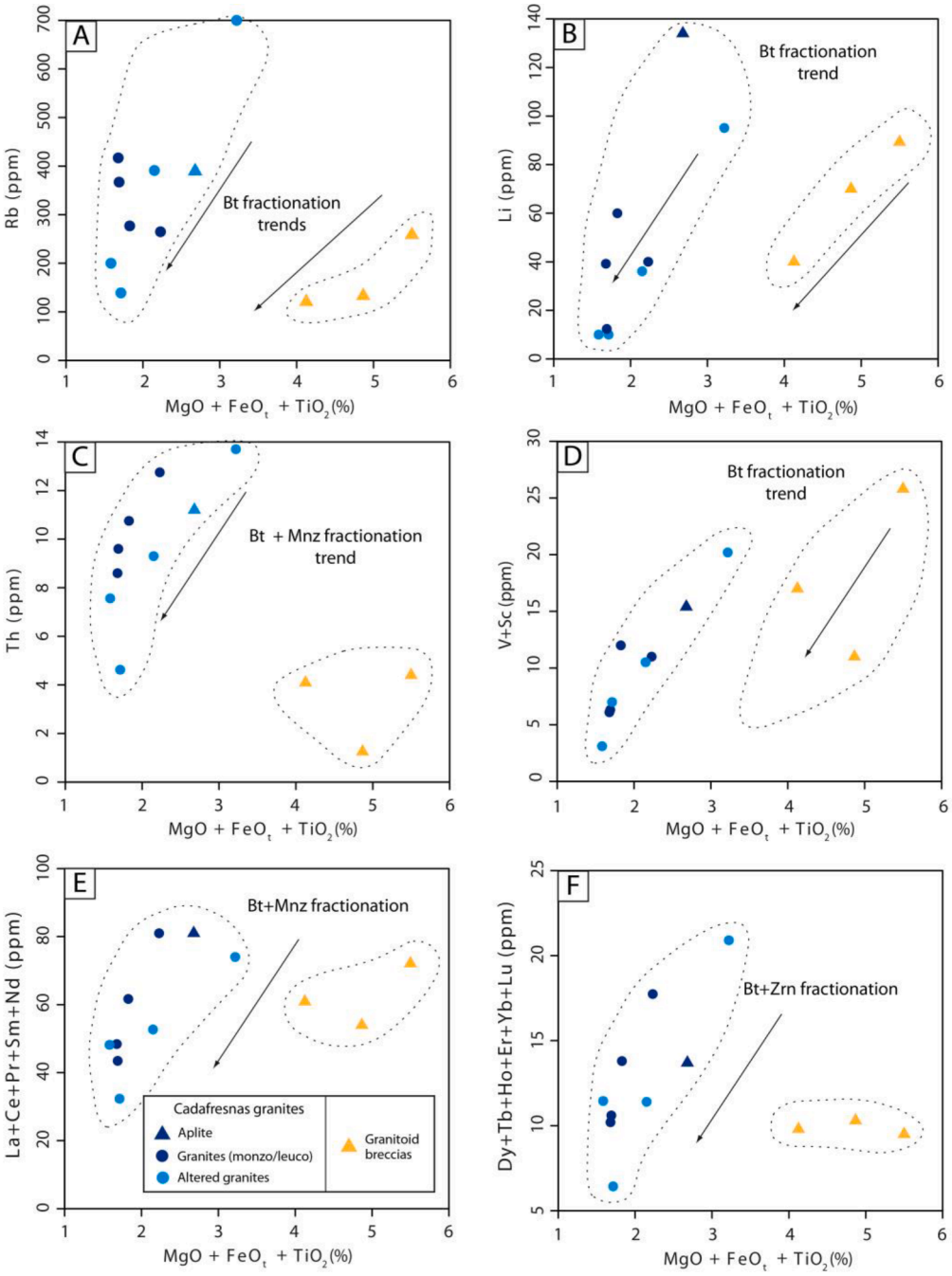

Fig. 5. Binary diagrams of maficity (B1 = MgO + FeO_t + TiO_2) vs the content of different trace elements and REE. The arrows indicate the expected biotite fractionation trends which cause a decrease of the maficity. Bt: biotite; Mnz: monazite; Zrn: zircon.

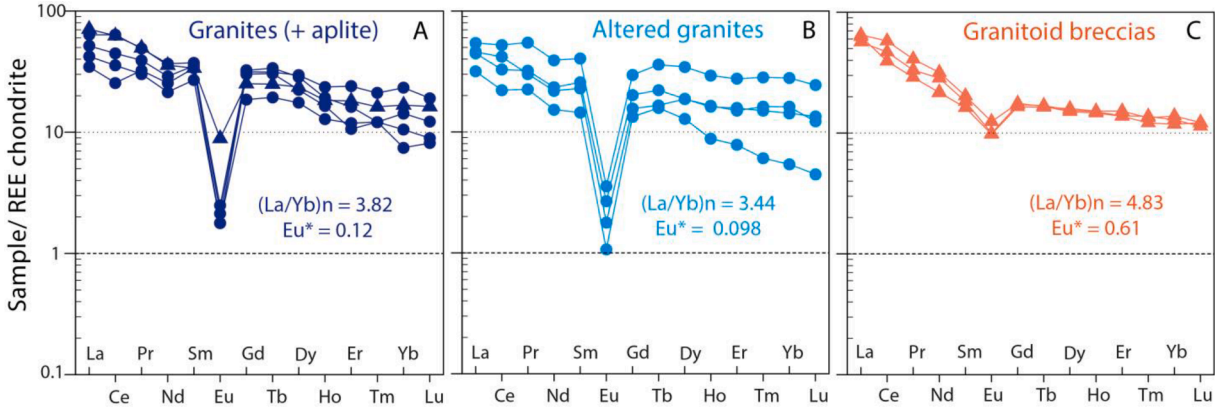

Fig. 6. Rare earth element (REE) diagram for the igenous rocks in Peña do Seo normalized to the chondrite values of McDonough and Sun (1995). A) Cadafresnas granites (and aplite, represented by triangles); B) altered Cadafresnas granites and C) granitoid breccias. Mean values of La/Yb ratio and Eu anomaly are given. Eu* is the Eu anomaly ($Eu^* = Eu_n/[Sm_n \times Gd_n]^{0.5}$) where n stands for normalized.

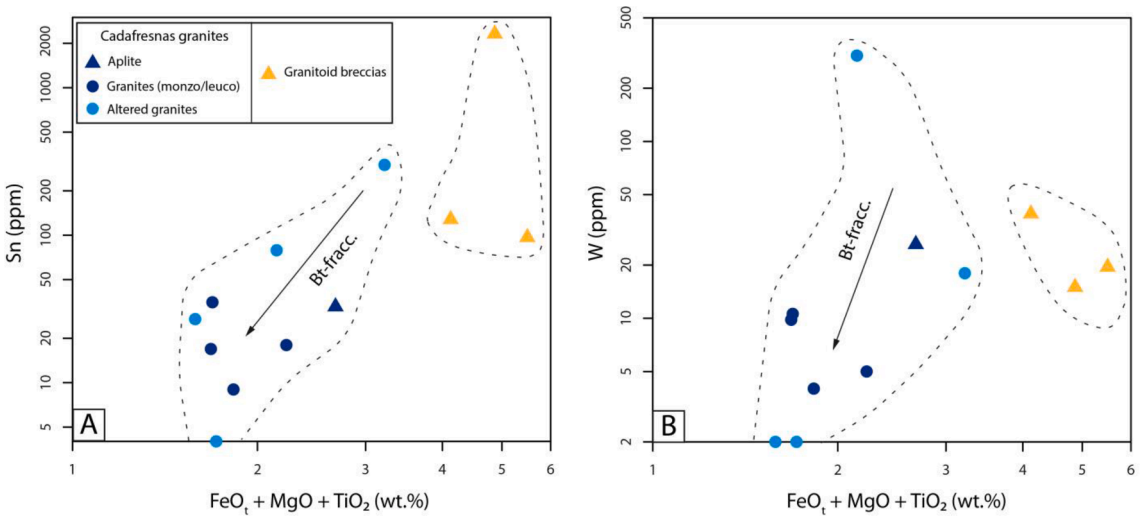

Fig. 7. $FeO_t + MgO + TiO_2$ vs Sn (A) and W (B). Different trends can be seen for the two big groups of igneous rocks. Sn and W show a similar behavior.

With the aim of characterizing the alteration of the different rocks, we used the Ishikawa Alteration Index of Ishikawa et al. (1976) and the Chlorite-Carbonate-Pyrite Index of Large et al. (2001) (Fig. 8). Granitoid breccias plot in the least altered boxes of mafic and intermediate rocks whereas the granites show a chloritic-sericitic alteration trend, which is consistent with the observed alteration of K-feldspar to sericite.

4.3. Mineralogy and paragenesis

Based on textural observations in host rocks, granitoid breccias and the mineralized quartz veins, a sequence of the different mineral associations or paragenesis (paragenetic diagram) has been produced for the Peña do Seo deposit (Fig. 9). It consists of a pre-ore stage dominated by host-rock alteration, three hypogene ore stages and a supergene alteration stage.

Stage 0: pre-ore stage: Host rock alteration (Figs. 10, 11A). This stage is mainly characterized by pervasive tourmalinization of the pyrite (Py-0)-bearing host schist (Figs. 10A–D, 11A) close to the quartz veins, along with biotite. Tourmaline found within the schist is more abundant near the contact with the quartz veins (~10 cm). Tourmaline grains are euhedral and between 50 and 400 μm in size. Biotite appears as nodules between 50 and 250 μm in size, and is occasionally overgrown by tourmaline (Fig. 10C–D).

Ore Stage I: oxide-halide-sulfide stage (Figs. 11–12). During this stage, the intrusion of granitoids of brecciated appearance took place. They are composed of K-feldspar and abundant fluorite and muscovite (Fig. 11E), with a first generation of cassiterite (Cst I, Fig. 11C, 12A), some pyrite (Py I, Figs. 11B,C,D,F,G, 12A) and minor arsenopyrite (Apy I, Fig. 11B) and chalcopyrite (Ccp I), as well as altered fragments of the host quartz schists. Tourmaline, rutile (Fig. 11F), a Pb-Bi-Ag sulfosalt (Fig. 12B) and waylandite (Fig. 12F) are also present. Py-I forms subidiomorphic to idiomorphic crystals between 50 and 500 μm in size (Fig. 11G), whereas arsenopyrite forms smaller crystals, between 10 and 100 μm, also subidiomorphic to idiomorphic in shape (Fig. 11B). Intergrowths of pyrite-arsenopyrite are found, indicating they are coeval. Cst I forms brownish crystals between 200 μm and 800 μm and shows a clear oscillatory zonation. Fluorite forms crystals between 300 μm and several cm. Chalcopyrite (Ccp I) is also found in this stage. The Pb-Bi-Ag sulfosalt is mainly found filling cracks in pyrite (Fig. 12B), and locally, native bismuth and waylandite overgrow arsenopyrite (Apy I; Fig. 12F).

Ore Stage II: main oxide stage (Figs. 11–12). During this stage, a selvage is developed between the veins and the host rock, mainly composed of muscovite (Ms I), prehnite (Prh I), apatite and wolframite (Wf I, Fig. 11H). In the vein itself, a second generation of wolframite (Wf II, Figs. 11I, 12C) and minor amounts of cassiterite (Cst II, Fig. 12D) are found within the first generation of quartz (Qtz I). Qtz I is massive, characterized by its milky appearance, coarse grain size (>500 μm) and uniform extinction (very locally, some of the crystals show undulose

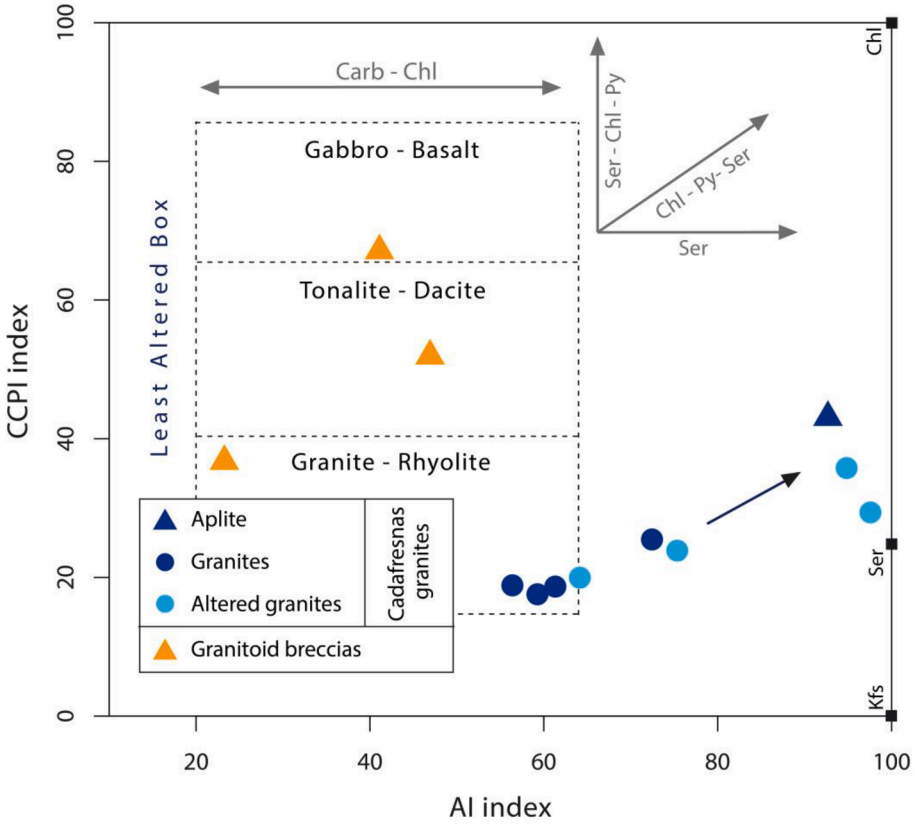

Fig. 8. A) AI-CCPI diagram with the least alteration boxes for mafic, intermediate and felsic composition (Large et al., 2001; Gifkins et al., 2005). Alteration indexes are CCPI = Chlorite-Carbonate-Pyrite Index: 100 × (FeO + MgO) / (FeO + MgO + Na_2O + K_2O); and AI = Ishikawa Alteration Index: 100 × (MgO + K_2O) / (MgO + K_2O + CaO + Na_2O). Carb: carbonate; Chl: chlorite; Ser: sericite; Py: pyrite; Kfs: K-feldspar.

Stages		0: Pre-ore	I: oxides-halides-sulfides	II: main oxide stage (selvage and veins)	III: main sulfide stage (veins)	IV: Supergene
Mineral	Formula	Host-rock alteration	Sn-F-Bi-REE-Fe	W-Sn-(Mo)	Fe-As	
Biotite	$K(Mg,Fe)_3(AlSi_3O_{10})(F,OH)_2$					
Tourmaline	$AD_3G_6(T_6O_{18})(BO_3)_3X_3Z$					
Muscovite	$KAl_2(AlSi_3O_{10})(OH)_2$					
Arsenopyrite	FeAsS					
Chalcopyrite	$CuFeS_2$					
Cassiterite	SnO_2					
Pyrite	FeS_2					
Fluorite	CaF_2					
K-feldspar	$KAlSi_3O_8$					
Rutile	TiO_2					
Bi-Pb-Ag sulfosalt	$Ag_3Pb_8Bi_{11}S_{26}$					
Waylandite	$BiAl_3(PO_4)_2(OH)_6$					
Native bismuth	Bi					
Quartz	SiO_2					
Prehnite	$Ca_2Al_2Si_3O_{10}(OH)_2$					
Wolframite	$(Fe/Mn)WO_4$					
Molybdenite	MoS_2					
Apatite	$Ca_5(PO_4)_3(Cl/F/OH)$					
Chlorite	$(Mg,Fe)_3(Si,Al)_4O_{10}(OH)_2 \cdot (Mg,Fe)_3(OH)_6$					
Stannite	Cu_2FeSnS_4					
Ilmenite	$Fe^{2+}TiO_3$					
Sphalerite	ZnS					
Scorodite	$Fe^{3+}AsO_4 \cdot 2H_2O$					
Covellite	CuS					

Fig. 9. Paragenetic sequence in host rocks, granitoid breccias and the mineralized quartz veins of Peña do Seo deposit.

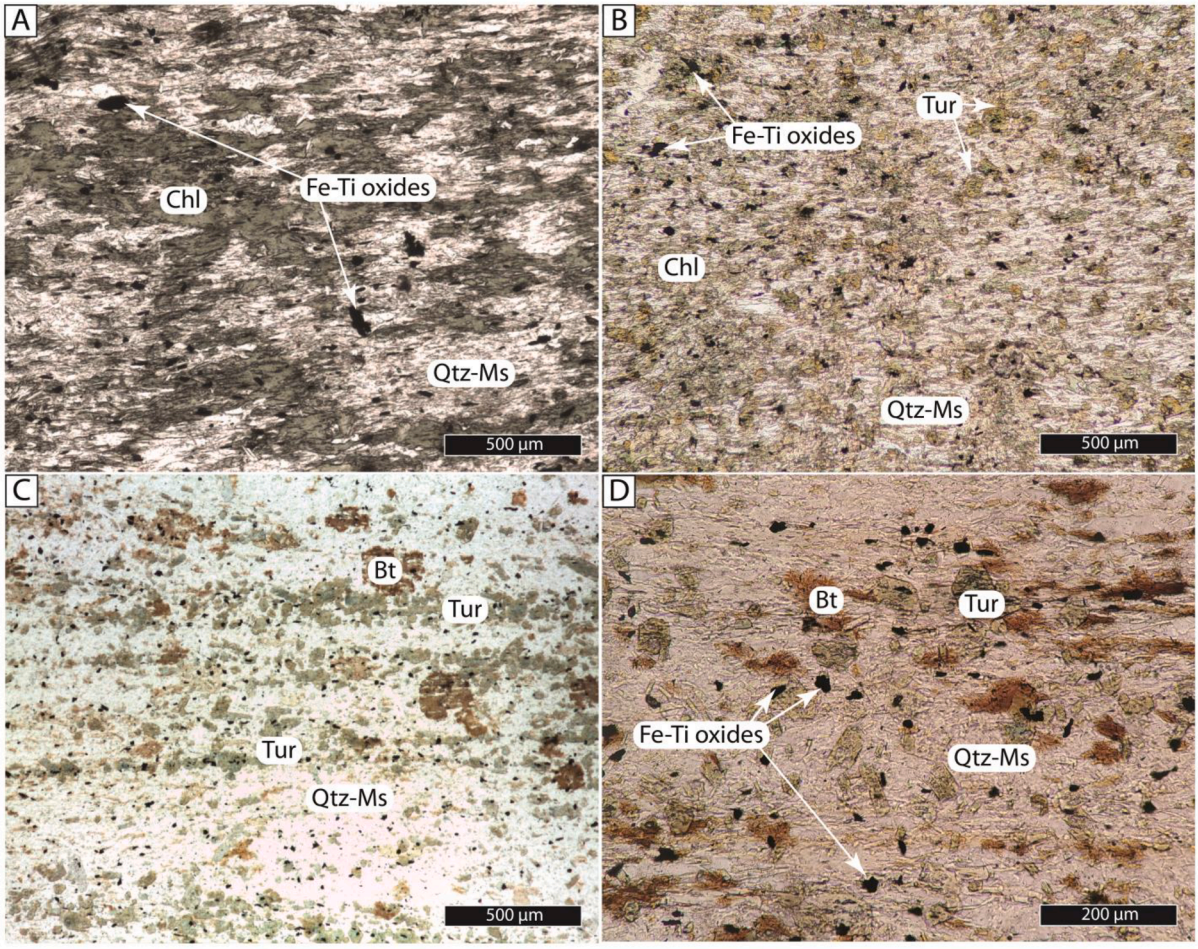

Fig. 10. Microphotographs of the host quartz schist. A) Aspect of the unaltered schist, far from the igneous rocks and the quartz veins, showing a composition of quartz, muscovite, chlorite and Fe-Ti oxides as accesory. B) Quartz schist showing spotted texture with tourmaline crystals (Tur), chlorite (Chl), quartz (Qtz), muscovite (Ms) and accessory Fe-Ti oxides. C) and D) Quartz schist spotted with biotite (Bt) nodules, result of contact metamorphism, overgrown by tourmaline crystals (Tur) as a result of flowing fluids close to a quartz vein (~10 cm), in a matrix of abundant quartz (Qtz), and muscovite (Ms), with Fe-Ti oxides as accessory. All pictures in transmitted light and parallel nicols.

extinction). Wf I forms crystals between 200 µm and 2 cm, whereas Wf II forms elongated crystals 20 µm-3 cm long. Cst II forms crystals between 300 and 600 µm and shows oscillatory zonation. Minor amounts of molybdenite (Mo, Fig. 12D–E) form 10–30 µm long acicular crystals.

Ore Stage III: main sulfide stage (Figs. 11–12). During the third stage, abundant pyrite (Py II) and minor arsenopyrite and chalcopyrite precipitated along with a second generation of quartz (Qtz II), together with abundant chlorite, which is overgrown by a second generation of apatite (Fig. 11J). Qtz II is granoblastic and shows uniform extinction. Pyrite appears as subhedral crystals, often massive, and filling cracks in quartz II. Pyrite (Py II) masses appear very commonly embedded in chlorite patches, and overgrow apatite, arsenopyrite and chalcopyrite (Fig. 11J). Stannite (Stn) forms crystals between 50 µm and 200 µm, often replacing cassiterite (Cst II, Fig. 12G). Locally, rutile (Rt II) overgrows stannite (Fig. 12G), and isolated crystals of sphalerite and ilmenite overgrow chlorite (Fig. 12H).

Ore Stage IV: supergene stage (Fig. 12). Mineral assemblages from the three previous stages are locally replaced by supergene minerals. Chalcopyrite is replaced by covellite and arsenopyrite is replaced by scorodite (Fig. 12I).

4.4. Fluid characterization

4.4.1. Petrography, distribution and types of fluid inclusions

In Peña do Seo, Qtz I and Qtz II commonly present suitable fluid inclusions for microthermometric and Raman microspectrometry studies. In contrast, appropriate fluid inclusions for microthermometry have not been found in other minerals of interest, such as cassiterite, wolframite or fluorite, as they were too small to be analyzed. Around 200 fluid inclusions have been selected in vein quartz crystallized during stages II and III. They are commonly small in size (<10 µm). Cathodoluminescence was performed in the different types of quartz (Qtz I, co-precipitated with wolframite and cassiterite (Fig. 13A,C), and Qtz II, co-precipitated with sulfides; Figs. 9, 13E,G) to determine the paragenetic significance of the studied fluid inclusion assemblages and to identify quartz textures (Fig. 13). Qtz I appears as massive crystals and show growth zoning, with blue colors (Fig. 13B,D), whereas Qtz II forms polygonal grains with no color zoning (Fig. 13F,H). No signs of deformation were found in quartz grains.

Different fluid inclusions assemblages (FIAs) were defined, according to the occurrence and the spatial relationship of the fluid inclusions, their characteristics at room temperature and their behavior during microthermometric cycles (Fig. 14, Table 2). Then, the selected fluid inclusions were regrouped into three different types (I, II, III; Table 3). Type I consists of rounded to slightly elongated two-phase isolated aqueous fluid inclusions, with sizes between 3 and 7 µm and degrees of fill (F) between 0.8 and 0.6, hosted by quartz I in stage II quartz-wolframite-cassiterite veins. Following the criteria of Roedder (1984), they are presumably primary, as they appear isolated and show a random distribution (Fig. 14A-D). Type II consists of three-phase

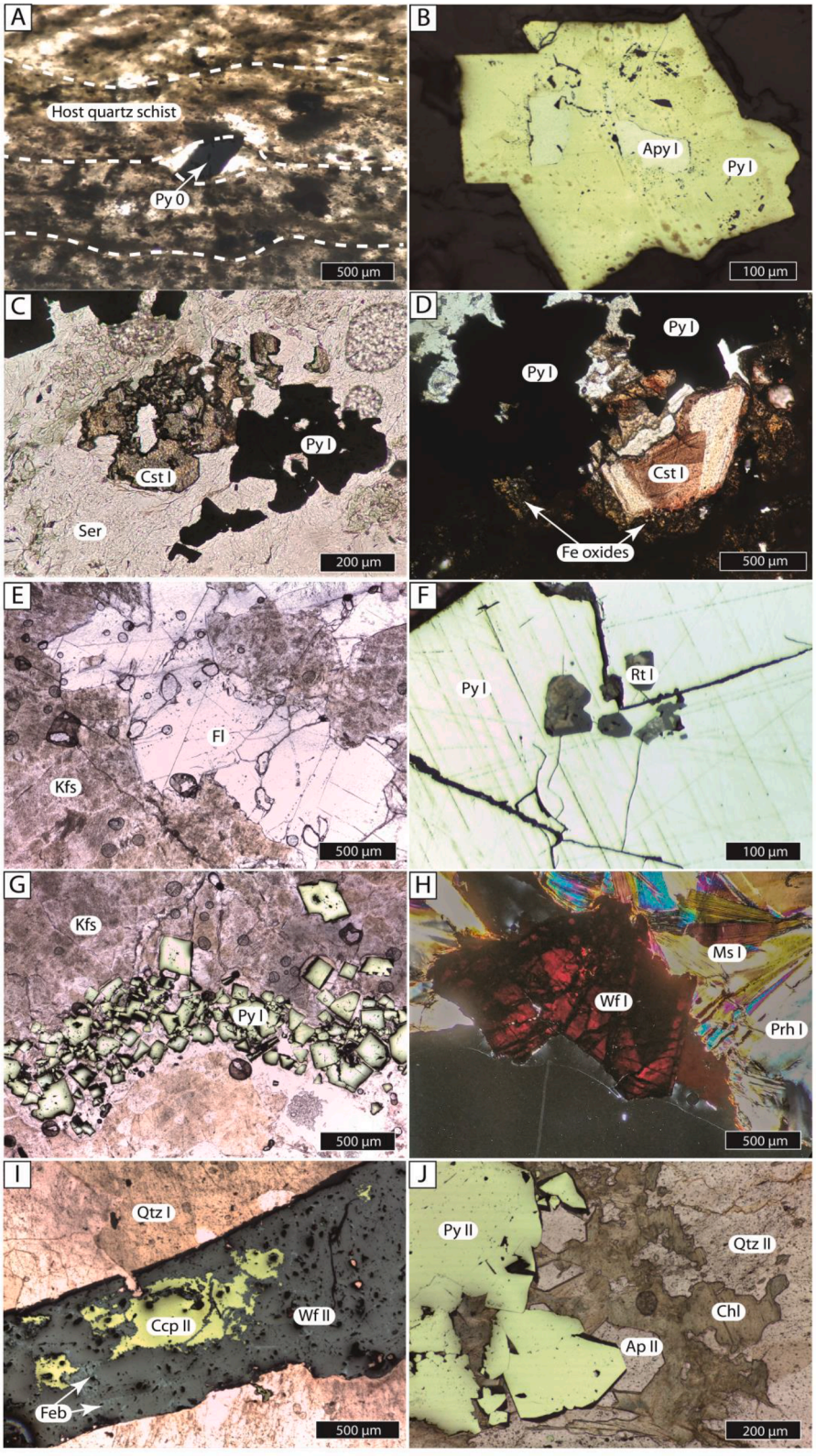

Fig. 11. Optical microscopy images of mineralization in Peña do Seo. A) Pre-kinematic pyrite (Py 0) in host quartz schist. B) Pyrite (Py I)-arsenopyrite (Apy I) intergrowth in granitoid breccia (stage I). C) Cassiterite (Cst I) and pyrite (Py I) in granitoid breccia (stage I). D) Cassiterite (Cst I) overgrown by pyrite (Py I) and Fe oxides in granitoid breccia (stage I). E) Fluorite (Fl) mineralization overgrown by K-feldspar (Kfs) in granitoid breccia (stage I). F) Inclusions of rutile (Rt) in pyrite (Py I) from granitoid breccias. G) Subhedral to euhedral pyrite (Py I) in a K-feldspar (Kfs) matrix. H) Wolframite (Wf I) overgrown on muscovite (Ms I) and Prehnite (Prh I) in vein selvage. I) Wolframite (Wf II) in quartz (Qtz I) vein is partly overgrown by chalcopyrite (Ccp II) and ferberite (Feb). J) Subhedral pyrite crystals (Py II) overgrown on chlorite (Chl) and apatite (Ap) in a quartz (Qtz II) vein, stage III. A, C, D, E, H: transmitted reflected light; B, F, G, I, J: transmitted light. A, C, D, E, F: parallel nicols; B: crossed nicols.

rounded to oval isolated aqueous-carbonic fluid inclusions, with sizes between 2 and 10 µm and F between 0.7 and 0.4, hosted by quartz II in stage III sulfide-rich veins (Fig. 14B–C). As they show a very similar distribution to type I fluid inclusions, they are considered to be of primary origin as well. Type III are aqueous two-phase fluid inclusions hosted by quartz (both Qtz I and Qtz II) in veins from stage II and III, with F between 0.7 and 0.5. They are elongated and mostly irregular in shape, and 8 to 20 µm in size. They often form intercrystalline trails, sometimes following fractures, which indicates that they are secondary in origin (Fig. 14D–G). No evidences of fluid reequilibration (stretching,

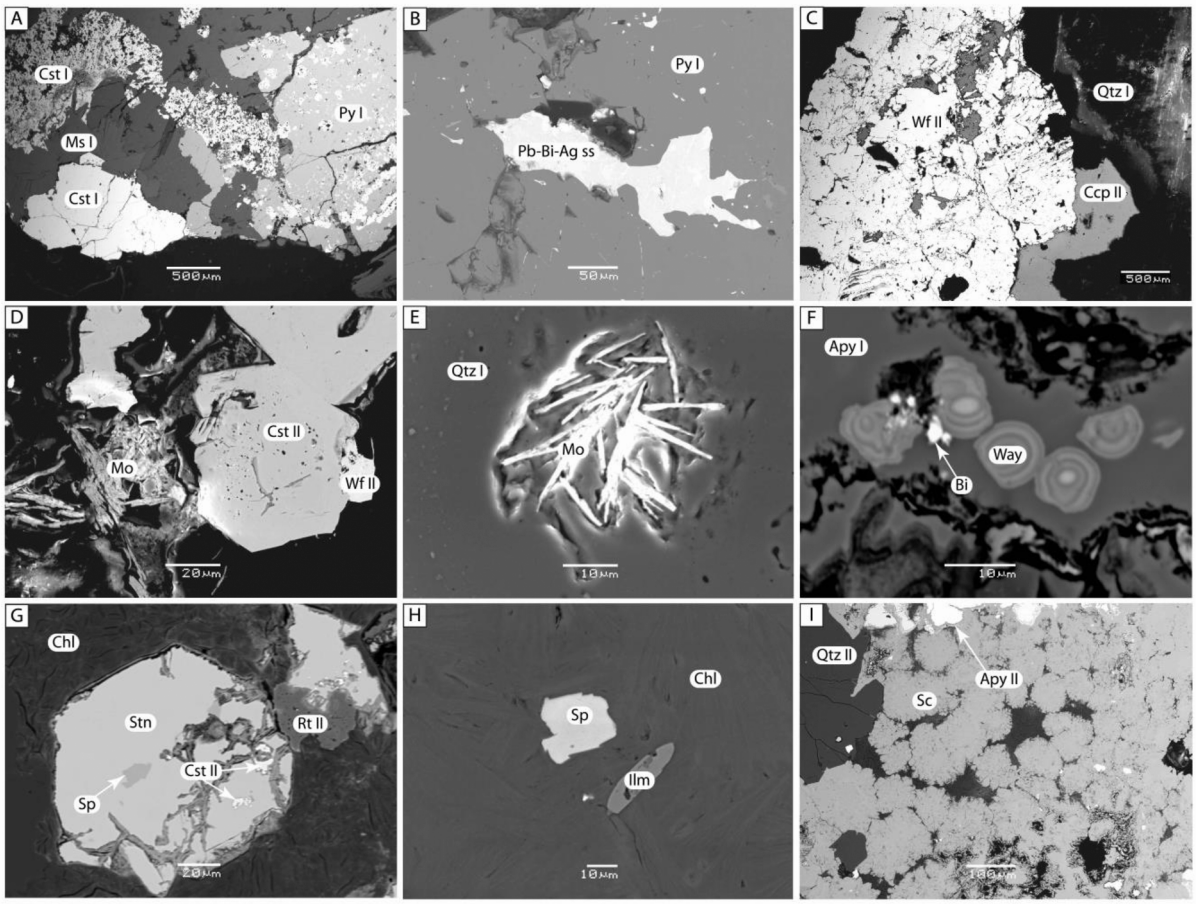

Fig. 12. Back-scattered electron (BSE) images of mineralization in Peña do Seo. A) Cassiterite, (Cst I and Cst II) pyrite (Py I) and muscovite in granitoid breccia. B) Pb-Bi-Ag sulfosalt (Pb-Bi-Ag ss) filling cracks in pyrite (Py I) in granitoid breccia. C) Wolframite crystal (Wf II) with chalcopyrite both surrounding and replacing it. D) Economic minerals found in the quartz veins: cassiterite I (Cst I), wolframite (Wf II) and molybdenite (Mo). E) Molybdenite (Mol) in a quartz vein. F) Waylandite (Way) and native bismuth (Bi) overgrowing arsenopyrite (Apy I). G) Stannite (Stn) with inclusions of cassiterite (Cst II) and sphalerite (Sp), Stannite is overgrown by rutile. H) Sphalerite (Sp) and ilmenite (Ilm) surrounded by chlorite (Chl) in sulfide-rich quartz (Qtz II) veins.I) Aggregates of framboidal scorodite (Sc). Some arsenopyrite (Apy) crystals are visible at the top edge, within a sulfide-bearing quartz (Qtz II) vein.

leakage, decrepitation) were found among the fluid inclusions studied.

4.4.2. Microthermometric and Raman microspectrometry results

Microthermometric and Raman microspectrometry data of the fluid inclusion assemblages (FIAs) are summarized in Table 2 with all abbreviations used in the text.

Type I fluid inclusions, which are aqueous (H_2O-NaCl), yield ice melting temperatures (Tm_{ice}) between −9.8 °C and −5.9 °C corresponding to salinities between 13.7 and 8.8 wt% NaCl eq. Homogenization temperature (Th) occurs to the liquid phase at temperatures between 288 °C and 442 °C (Table 3). Their density is between 0.90 and 0.55 g/cm^3. Type II fluid inclusions (H_2O-CO_2-N_2-CH_4-NaCl) are hosted by quartz II and show Th ranging from 261 °C to 339 °C (Figs. 15, 16). The Tm_{CO2} is between −57.6/-56.6 °C, clathrate melting temperature (Tm_{Cl}) is between 7.3 °C and 9 °C, and salinities are between 1.9 and 6.2 wt% NaCl. eq. Volatile phase composition is dominated by CO_2 (87.3–100 %), with lower amounts of N_2 (1.4–3.5 %) and CH_4 (0.2–3.8 %). Their density is between 0.96 and 0.40 g/cm^3. Type III fluid inclusions (H_2O-NaCl) yield homogenization temperatures between 274 °C and 155 °C and Tm_{ice} between −3.6 °C and 0 °C with corresponding salinities between 5.9 and 0.0 wt% NaCl eq.

4.5. Stable isotope data

4.5.1. Oxygen and hydrogen isotopes

$\delta^{18}O$ isotopic signatures were obtained in quartz, muscovite and chlorite from granite, metamorphic host rocks and quartz veins and their selvages (Table 4, Fig. 17). δD were obtained for biotite, muscovite and chlorite from the same rocks (Table 4). Qtz I yields the highest $\delta^{18}O$ values, from 12.0 ‰ to 13.2 ‰, whereas $\delta^{18}O$ of Qtz II ranges between 13.0 ‰ and 13.6 ‰. Quartz from Cadafresnas granite has values between 12.1 ‰ and 12.3 ‰. The lowest $\delta^{18}O$ values, between 11.2 ‰ and 11.5 ‰, correspond to late quartz veins crosscutting the granite (Fig. 17).

δD values range between −111.5 ‰ and −105.3 ‰ for biotite, between −74.3 ‰ and −71.5 ‰ for muscovite from stage I granitoid breccias, between −86.3 ‰ and −71.7 ‰ for muscovite from stage II, and between −69.4 ‰ and −67.1 ‰ for chlorite from stage III (Table 4).

4.5.2. Sulfur isotopes

$\delta^{34}S$ analyses were performed in pyrite, arsenopyrite and chalcopyrite from the granitoid breccias and quartz veins and also in pyrite found in the host Neoproterozoic quartz schists. The results show a great variability. $\delta^{34}S$ values in the pyrite found in the quartz schists (Py 0) range between +17.4 ‰ and +18.6 ‰. In granitoid breccias, $\delta^{34}S$ ranges between +13.0 ‰ and +14.2 ‰ for Py I, between 15.0 ‰ and 15.2 ‰ for arsenopyrite and between +13.0 ‰ and +13.6 ‰ for chalcopyrite. $\delta^{34}S$ values in massive

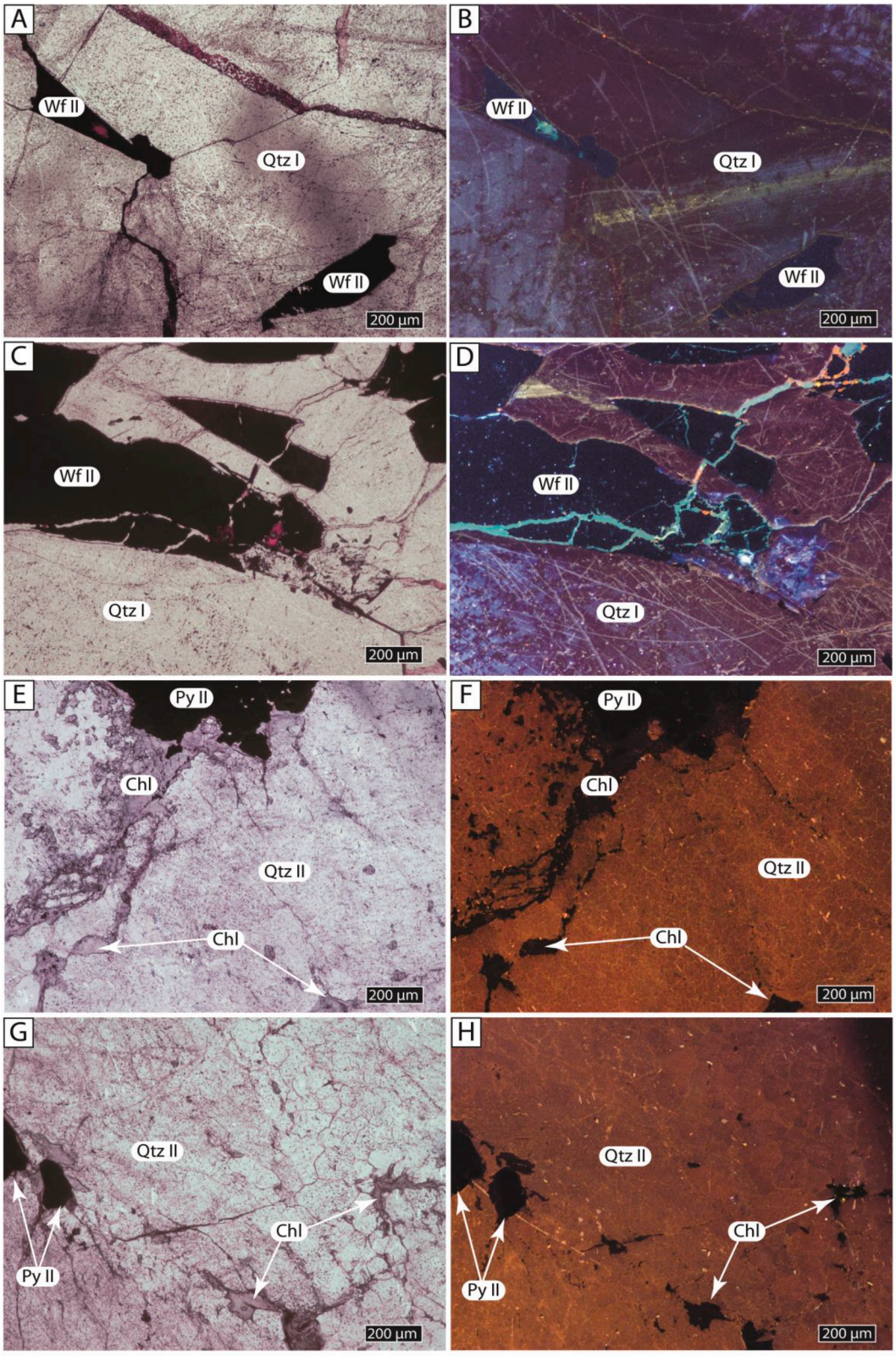

Fig. 13. Petrographic (A, C, E, F; parallel nicols) and cathodoluminescence (CL) microphotographs (B, D, F, H) of quartz co-precipitated with wolframite (Qtz I) and sulfides (Qtz II). Growth zoning can be seen in quartz I. Qtz: quartz; Wf: wolframite; Py: pyrite; Chl: chlorite.

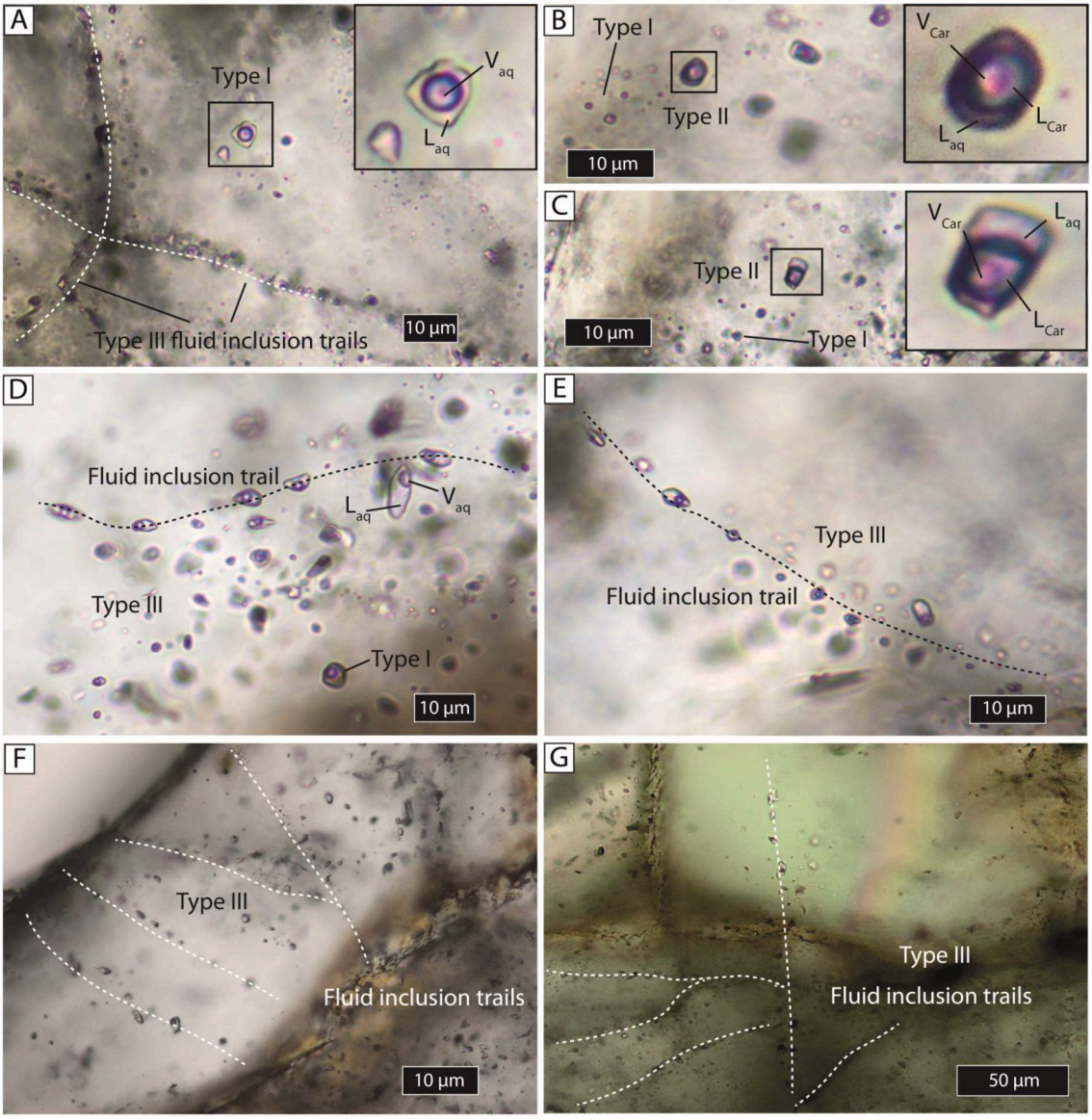

Fig. 14. A) Type I two-phase primary isolated aqueous fluid inclusion and trail of secondary aqueous fluid inclusions. B) and C) Type II primary isolated three-phase aqueous-carbonic fluid inclusions coexisting with Type I aqueous fluid inclusions. D) Type I inclusion and Type III secondary fluid inclusion trail. E), F), G) Secondary Type III fluid inclusion trails.

Table 2
Microthermometric data for the fluid inclusion assemblages (FIAs) in Peña do Seo.

	FIA	n	Type	Stage	Host	Comp.	Origin	FV (%)	Tm_{CO2}(°C)	Tm_{Cl}(°C)	Tm_{ice}(°C)	Th_{CO2}(°C)	Th(°C)	NaCl (wt.% eq.)	Global density (g/cm^3)
1	1-1b1	7	I	II	Qtz I	H_2O-NaCl	P	40/20	–	–	−8.2/-7.2	–	370.8/352.7	11.9/10.7	0.73/0.61
2	1-1e	3	I	II	Qtz I	H_2O-NaCl	P	40	–	–	−8.1/-7.2	–	431.4/419.0	11.6/11.2	0.66/0.55
3	1-1f	3	I	II	Qtz I	H_2O-NaCl	P	40	–	–	−8.3/-7.2	–	335.4/313.4	12.0/10.7	0.90/0.87
4	1–1 g	7	I	II	Qtz I	H_2O-NaCl	P	50/30	–	–	−7.5/-6.1	–	442.6/412.1	11.1/9.3	0.60/0.56
5	21-1b	4	I	II	Qtz I	H_2O-NaCl	P	40/30	–	–	−9.1/-8.4	–	328.7/307.8	13.0/12.2	0.87/0.82
6	21-2a2	3	I	II	Qtz I	H_2O-NaCl	P	30	–	–	−6.6/-6.2	–	378.2/368.0	13.4/9.5	0.71/0.69
7	21-2a3	4	I	II	Qtz I	H_2O-NaCl	P	30			−9.8/-9.2	–	310.4/299.5	13.7/13.1	0.87/0.78
8	21-3c1	6	I	II	Qtz I	H_2O-NaCl	P	40/30	–	–	−9.8/-7.1	–	378.1/331.9	13.2/10.6	0.82/0.72
9	21-5d	8	I	II	Qtz I	H_2O-NaCl	P	40/20	–	–	−6.8/-6.0	–	354.5/294.7	10.2/9.2	0.86/0.74
10	21-5e	4	I	II	Qtz I	H_2O-NaCl	P	30/20	–	–	−8.2/-6.0	–	304.1/288.4	11.9/9.2	0.86/0.81
11	6-1b	4	I	II	Qtz I	H_2O-NaCl	P	40	–	–	−8.2/-7.2	–	306.1/298.3	11.3/10.3	0.85/0.83
12	6-1c	7	I	II	Qtz I	H_2O-NaCl	P	50/40	–	–	−8.3/-6.1	–	315.2/297.7	11.4/9.1	0.84/0.81
13	6-2a	5	I	II	Qtz I	H_2O-NaCl	P	50	–	–	−8.4/-6.2	–	315.0/312.9	11.5/9.2	0.83/0.80
14	6-2b	9	I	II	Qtz I	H_2O-NaCl	P	40	–	–	−8.3/-5.9	–	314.8/294.9	11.4/8.8	0.86/0.80
15	6-2c	4	I	II	Qtz I	H_2O-NaCl	P	40/30	–	–	−9.0/-8.2	–	316.1/311.5	12.0/11.3	0.84/0.83
16	6-1a	3	II	III	Qtz II	H_2O-NaCl-CO_2-CH_4-N_2	P	60/40	−56.6	9.0/8.8	–	27.1/25.3	317.8/288.4	4.9/4.2	0.96
17	21-1f	2	II	III	Qtz II	H_2O-NaCl-CO_2-CH_4	P	60	−57.6/-57.5	9.0/8.8	–	28.0/27.8	291.5/285.2	5.9/4.9	0.92/0.85
18	21–1g	2	II	III	Qtz II	H_2O-NaCl-CO_2-CH_4	P	60	−57.5/-56.6	8.8/8.2	–	28.2/26.3	316.4/261.9	2.9/1.9	0.4
19	21-3b	7	II	III	Qtz II	H_2O-NaCl-CO_2-CH_4	P	70/60	−57.4/-57.1	8.8/7.3	–	27.9/26.2	333.9/316.4	7.3/3.8	0.96/0.92
20	21-3c2	3	II	III	Qtz II	H_2O-NaCl-CO_2-CH_4	P	70	−57.0/-56.8	8.4/8.3	–	26.9/26.5	303.2/262.4	5.7/5.3	0.96/0.95
21	21-5a	4	II	III	Qtz II	H_2O-NaCl-CO_2-CH_4-N_2	P	60/40	−56.9/-56.7	8.7/8.5	–	25.5/25.3	339.3/300.5	5.6	0.96/0.4
22	21-5b	3	II	III	Qtz II	H_2O-NaCl-CO_2-N_2	P	70/60	−56.8/-56.6	8.7/8.6	–	28.4/28.3	307.1/299.8	6/5.8	0.91/0.4
23	21-5e	5	II	III	Qtz II	H_2O-NaCl-CO_2 -CH_4-N_2	P	50/40	−56.9/-56.6	8.6/8.5	–	25.3/23.9	326.7/295.4	5/4.14	0.93/0.92
24	21-5f1	4	II	III	Qtz II	H_2O-NaCl-CO_2 -CH_4-N_2	P	60	−56.8/-56.7	8.3	–	27.9/27.7	320.4/309.5	6.0/5.1	0.92/0.91
25	21-5f2	3	II	III	Qtz II	H_2O-NaCl-CO_2 -CH_4-N_2	P	60	−56.9/-56.6	8.7/8.3	–	27.2/26.5	333.8/318.6	6.2/5.3	0.95/0.93
26	21-6b	6	III	–	Qtz I / II	H_2O-NaCl	S	40	–	–	−2.8/-0.7	–	212.8/197.4	4.6/1.2	0.90/0.86
27	21-6c	4	III	–	Qtz I / II	H_2O-NaCl	S	40/30	–	–	−2.5/-2.1	–	188.5/175.1	4.2/3.5	0.92/0.9
28	1-1b2	10	III	–	Qtz I / II	H_2O-NaCl	S	40/20	–	–	−2.9/-2.6	–	219.4/187.8	4.8/4.3	0.92/0.86
29	1-1d	8	III	–	Qtz I / II	H_2O-NaCl	S	30	–	–	−2.7/-2.5	–	274.4/261.2	4.4/4.1	0.82/0.61
30	21-1a	7	III	–	Qtz I /II	H_2O-NaCl	S	30	–	–	−0.7/-0.6	–	267.0/225.5	1.16/0.99	0.84/0.78
31	21-2a1	11	III	–	Qtz I / II	H_2O-NaCl	S	30/20	–	–	−0.6/0.0	–	217.7/205.8	1.05/0.0	0.94/0.91
32	21-2b	8	III	–	Qtz I / II	H_2O-NaCl	S	30/20	–	–	−3.6/-1.4	–	209.1/154.9	5.86/2.40	0.96/0.87
33	21-2c	7	III	–	Qtz I /II	H_2O-NaCl	S	30	–	–	−2.8/-2.6	–	172.8/168.9	4.6/4.3	0.93
34	21-2d	9	III	–	Qtz I /II	H_2O-NaCl	S	30/20	–	–	−2.9/-2.8	–	214.2/201.3	4.8/4.6	0.90/0.89

Table 3
Microthermometric and Raman data for the different types of fluid inclusions in Peña do Seo.

	Type I	Type II	Type III
Phase stage	Stage II	Stage III	Stage II and III
Mineral host	Quartz I	Quartz II	Quartz I and II
Composition	H_2O-NaCl	H_2O-NaCl-CO_2-CH_4-N_2	H_2O-NaCl
FV (%)	20/50	40/70	20/40
Microthermometry (°C)			
Tm_{CO2}	–	−57.6/-56.6	–
Tm_{Cl}	–	7.3/9.0	–
Tm_{ice}	−11.8/-5.7	–	−2.9/0.0
Th_{CO_2}	–	24.4/28.4 (L)	–
Th	284/442 (L)	262/339 (L)	157/267 (L)
Raman (mol %)			
ZCO_2	–	87.3/100	–
ZCH_4	–	0.2/3.8	–
ZN_2	–	1.4/3.5	–
Bulk composition (mol %)			
XH_2O	90.0/94.2	50.4/77.1	96.9/99.2
XN_2	–	0.0/1.9	–
XCO_2	–	19.2/47.8	–
XCH_4	–	0.0/0.8	–
NaCl	5.8/10.0	0.9/1.2	3.1/0.8
NaCl (wt.% eq.)	8.8/13.7	1.9/6.2	0.0/5.9
Global density (g/cm^3)	0.55/0.90	0.4/0.96	0.61/0.96

subhedral to anhedral pyrite (Py II) in chlorite-rich quartz veins from the third stage of mineralization yield much heavier S signatures, with $\delta^{34}S$ ranging from +35.1 ‰ to +38.0 ‰. (Table 5, Fig. 18).

5. Discussion

5.1. Origin of the granites and granitoid breccias related to the W-Sn deposits

The petrography and geochemistry of the studied igneous rocks suggest the existence of two different magmatic pulses: the Cadafresnas granites and the granitoid breccias, both related the Sn-W mineralization. The Cadafresnas granites (granites – including greisenized granites – and aplites) show features of S-type granites (e.g., its A/CNK vs. FeO_t + MgO + TiO_2 and Rb/Ba vs. Rb/Sr relations; Figs. 4, 19) (Chappell and White, 2001). A metasedimentary pelitic source and peritectic phases like sillimanite (Sill) ± cordierite (Crd)/garnet (Grt) could have been involved in the partial melting process (Villaseca et al., 1998; Clemens and Stevens, 2012). The high FeO_t/MgO, Na_2O + K_2O/CaO and Ga/Al of these granites could also indicate a minor A-type component in their source (Whalen, et al., 1987). The intrusion of these peraluminous magmas in the upper crustal levels involved biotite fractionation that caused part of the observed geochemical variation in diagrams shown in Fig. 5. Wolfram and Sn can be enriched in the granitic melts during the melting process (Zhao et al. 2021) but in this study case were subsequently depleted due to its possible compatibility with the biotite fractionation (Fig. 7).

The granitoid breccias are petrogenetically unrelated to the Cadafresnas granites. These rocks have low values of A/CNK (A parameter) and relatively high ones of FeO_t + MgO + TiO_2, thus being classified as

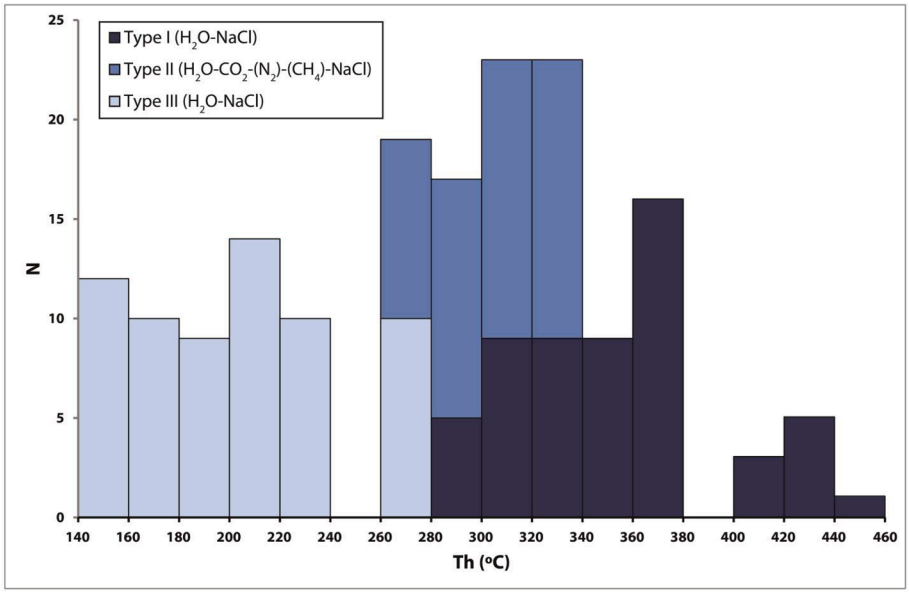

Fig. 15. Histogram of temperatures of homogenization (Th) for the three different types of fluid inclusions.

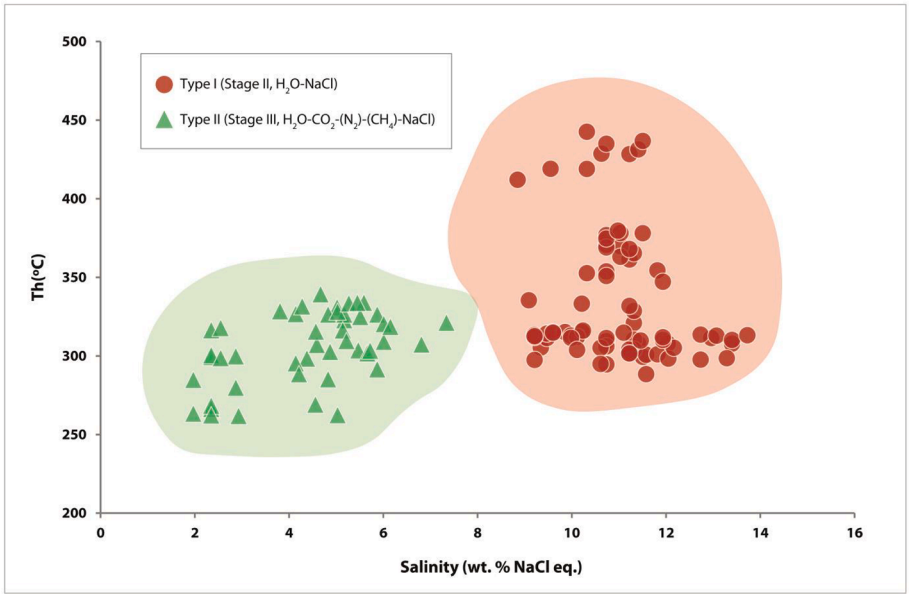

Fig. 16. Salinity vs temperature of homogenization (Th) plot for the two types of primary fluid inclusions.

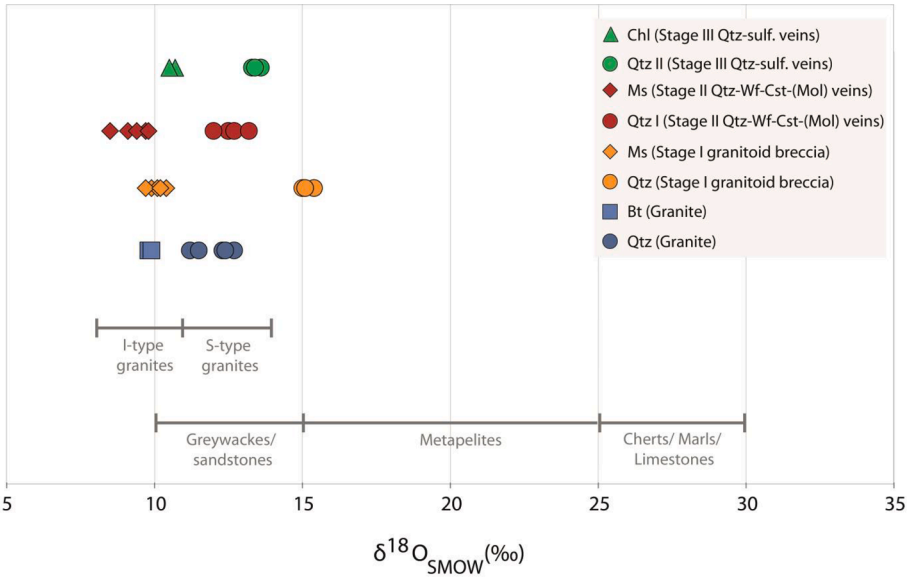

Fig. 17. $\delta^{18}O_{(SMOW)}$ data of minerals from different ore stages and granite. Most of the minerals show a likely magmatic origin, with the exception of quartz from granitoid breccia, which seems to have partially reequilibrated with host quartz schists.

metaluminous I-type granitoids (Fig. 4). Their Rb/Ba and Rb/Sr values indicate its derivation from partial melting of clay-poor, intermediate ± mafic greywackes (Fig. 19). Its elevated Ba, F and Sn contents could be explained by inputs of hydrothermal fluids and also by dehydration melting of biotite (±some other hydrated mafic phases) which could add such elements initially to the melt (Fernández-Suárez, 1994; Tischendorf et al., 2001; Villaros et al., 2009; Michaud et al., 2021; Zhao et al., 2021).

The W (±Sn) mineralization could have come from these crystallizing magmas, especially those of the granitoid breccias. Contact metamorphism could have activated dehydration reactions and circulation of fluids in the country rocks. This metamorphism generated the spotted schist (country rocks) that can be explained by muscovite/chlorite dehydration reactions (Ms-Pg + Qz = And + Ab + H_2O; Spear, 1993; Ms + Chl = And + Bt + Qz + H_2O; Pattison et al., 2011). Such reactions could have liberated W from its mineral host (e.g., muscovite; Michaud et al., 2021; Zhao et al., 2021) and given rise to W mineralization.

Table 4
O and H isotopic signatures from different stages of mineralization in Peña do Seo. Oxygen composition of fluids ($\delta^{18}O_{fluid}$): quartz (Qtz): Clayton et al., (1972), muscovite (Ms): O'Neil and Taylor (1967), biotite (Bt) and chlorite (Chl): Zheng (1993). Hydrogen composition of fluids (δD_{fluid}): biotite, muscovite: Suzuoki and Epstein (1976), chlorite: Graham (1984). Temperatures for veins were obtained from fluid inclusions. Temperature for granites and granitoids obtained from zircon saturation temperature (ZST) (Watson and Harrison, 1983).

Sample	Mineral	Rock	Stage	$\delta^{18}O$ (‰ SMOW)	δD (‰ SMOW)	H_2O	T_{min} (°C)	T_{max} (°C)	$\delta^{18}O_{fluid}$ min	$\delta^{18}O_{fluid}$ max	δD_{fluid} min	δD_{fluid} max
PS-7a	Bt	Qtz-Schist	0	+9.8	−111.5	8	280	435	5.9	8.4	−39.0	−61.7
PS-16	Bt	Granite	0	+9.9	−105.3	3.1	650	750	11.0	11.5	−77.5	−82.1
PS-12	Ms	Granitoid	I	+9.9	−71.5	0.9	620	631	10.8	10.9	−65.7	−66.8
PS-12	Ms	Granitoid	I	+10.2	−74.3	0.9	620	631	11.1	11.2	−62.9	−64.0
PS-2	Ms	W-Sn vein selvage	II	+9.7	−86.3	4.1	280	435	5.8	8.3	−33.1	−56.6
PS-2	Ms	W-Sn vein selvage	II	+9.1	−71.7	4.4	280	435	5.2	7.7	−18.5	−42.0
PS-7	Ms	W-Sn vein selvage	II	+9.4	−78.6	4.1	280	435	5.5	8.0	−25.4	−48.9
PS-7	Ms	W-Sn vein selvage	II	+9.8	−81.7	4	280	435	5.9	8.4	−28.5	−52.0
PS-21	Ms	Qtz-sulf. vein	III	+10.4	−99.6	4.3	260	340	6.0	7.9	−41.5	−59.7
PS-21	Ms	Qtz-sulf. vein	III	+10.1	−105.7	4.4	260	340	5.7	7.6	−47.6	−65.8
PS-21	Ms	Qtz-sulf. vein	III	+9.7	−80.7	2.4	260	340	5.3	7.2	−22.6	−40.8
PS-21	Ms	Qtz-sulf. vein	III	+10.2	−79	3.5	260	340	5.8	7.7	−20.9	−39.1
PS-21	Chl	Qtz-sulf. vein	III	+10.7	−67.1	2.1	260	340	6.3	8.2	−9.0	−27.2
PS-21	Chl	Qtz-sulf. vein	III	+10.5	−69.4	2.3	260	340	6.1	8.0	−11.3	−29.5
PS-16	Qtz	Granite	0	+12.3			650	750	11.7	12.5		
PS-18	Qtz	Granite	0	+12.7			650	750	12.1	12.9		
PS-16	Qtz	Granite	0	+12.4			650	750	11.8	12.6		
PS-20	Qtz	Granite	0	+11.2			650	750	10.6	11.4		
PS-20	Qtz	Granite	0	+11.5			650	750	10.9	11.7		
PS-12	Qtz	Granitoid	I	+15.0			620	631	14.2	14.3		
PS-12	Qtz	Granitoid	I	+15.4			620	631	14.6	14.7		
PS-12	Qtz	Granitoid	I	+15.1			620	631	14.3	14.4		
PS-1	Qtz	W-Sn vein	II	+12.5			280	435	4.8	8.4		
PS-2	Qtz	W-Sn vein	II	+12.7			280	435	5.0	8.6		
PS-4	Qtz	W-Sn vein	II	+12.0			280	435	4.3	7.9		
PS-7	Qtz	W-Sn vein	II	+13.2			280	435	5.5	9.1		
PS-21	Qtz	Qtz-sulp. vein	III	+13.3			260	340	4.9	7.7		
PS-21	Qtz	Qtz-sulp. vein	III	+13.6			260	340	5.2	8.0		
PS-21	Qtz	Qz-sulp. vein	III	+13.4			260	340	5.0	7.8		

Table 5
$\delta^{34}S$ (‰ V-CDT) sulfur isotope data for sulfides from Peña do Seo.

Sample	Mineral	$\delta^{34}S$ (‰ V-CDT)
PS-22	Py - host rock	+17.4
PS-22	Py - host rock	+17.5
PS-22	Py - host rock	+18.6
PS-22	Py - host rock	+18.1
PS-10	Py stage I	+13.0
PS-10	Py stage I	+13.1
PS-12	Py stage I	+14.2
PS-10	Apy stage I	+15.2
PS-10	Apy stage I	+15.0
PS-12	Apy stage I	+16.0
PS-1	Ccp stage I	+13.6
PS-1	Ccp stage I	+13.0
PS-21	Py stage III	+35.1
PS-21	Py stage III	+37.1
PS-21	Py stage III	+36.8
PS-21	Py stage III	+38.0
PS-21	Py stage III	+37.7

5.2. O-H-S isotopic signature in granites, granitoid breccias and quartz veins

$\delta^{18}O$ values higher than 10 ‰ have been previously described in Iberian peraluminous granites related to tin deposits (Fernández-Suárez, 1994; Chicharro et al., 2016), as well as in other granites from Western Europe (Hoefs and Emmermann, 1983; Jackson et al., 1989; Tartèse and Boulvais, 2010), and indicate that granites evolved from a sedimentary or metasedimentary protolith (Taylor, 1978), in agreement with their peraluminous geochemical signature (Chapter 4.3 in this paper). In Peña do Seo, $\delta^{18}O_{fluid}$ values decrease with decreasing temperatures obtained from fluid inclusions (quartz veins) and zircon saturation temperatures (ZST, granites; Watson and Harrison, 1983; Table 4), whereas δD values increase. The $\delta^{18}O$–δD plot shown on Fig. 20 includes the fields for the different types of waters (Sheppard, 1986; Ohmoto, 1986). $\delta^{18}O$ and δD data from fluids in equilibrium with minerals found in the granite (biotite), in the metamorphic aureola (biotite), in the granitoid breccias and in the veins from the different stages (muscovite, chlorite) are plotted. These $\delta^{18}O$–δD signatures indicate a fluid evolution from purely magmatic conditions in the granitoid breccias and the W-bearing veins towards contact metamorphic conditions in later sulfide-bearing veins. No input of meteoric fluids is observed (Fig. 20).

As for the $\delta^{34}S$ isotopic data, highly-positive $\delta^{34}S$ values (+13.0 ‰ to +37 ‰) are found in Peña do Seo sulfides. This indicates that marine sulfur, probably associated to deposition/diagenesis of the Neoproterozoic strata in a marine continental environment, could have been involved. $\delta^{34}S$ values from pyrite and arsenopyrite in granitoids (stage I) range between +13.4 ‰ and +15.2 ‰, thus indicating that the source of sulfur is not magmatic, and that sulfur was probably incorporated into the magma through melting and/or interaction with Neoproterozoic schists. Pyrite from the sulfide stage (Py-II, stage III) shows much heavier $\delta^{34}S$ values (+35.1 ‰ to +37.1‰), higher than most of the values obtained for sulfides in Northwestern Iberia (Gómez-Fernández et al., 2012; Martínez-Abad et al., 2015; Fuertes-Fuente et al., 2016). Higher values in NW Spain have only been reported for sulfides from orogenic gold deposits in the Truchas Syncline (Gómez-Fernández et al., 2021).

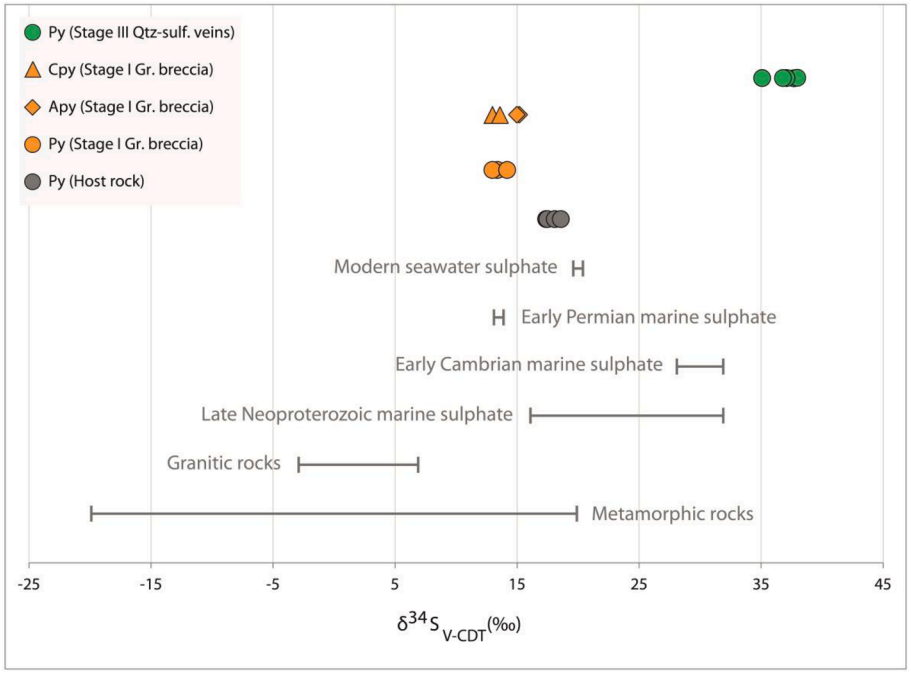

Fig. 18. $\delta^{34}S$ values of the sulfides in Peña do Seo. Data of global sulfides from Hoefs (2009). Data of marine sulfate from Claypool et al. (1980). V-CDT: Vienna-Canyon Diablo Troilite. Results show sources of sulfur are marine.

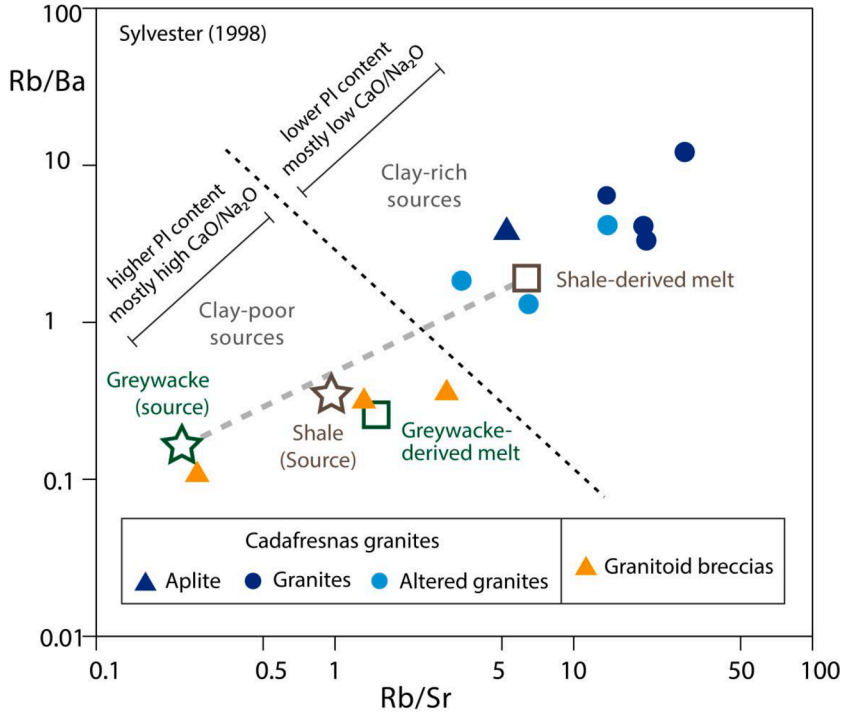

Fig. 19. Rb/Ba vs. Rb/Sr diagram after Sylvester (1998). The two magmatic pulses can be distinguished: i) Cadafresnas granites plot in the clay rich source field and close to the pelite-derived melt. ii) The granitoid breccias are closer to clay poor rocks.

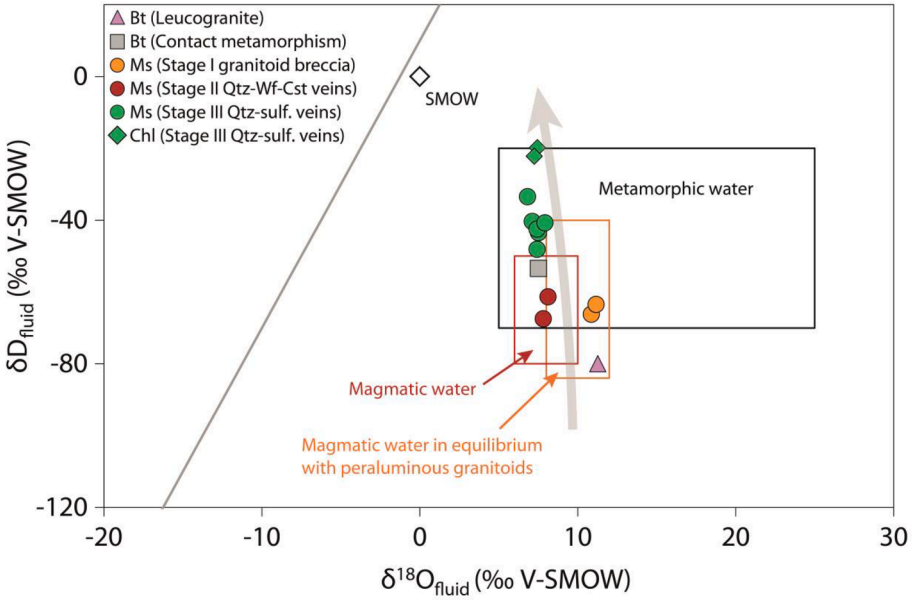

Fig. 20. $\delta^{18}O$–δD plot of the isotopic compositions of fluids in Peña do Seo and proposed fluid evolution according to ore stages (grey arrow). V-SMOW: Vienna Standard Mean Ocean Water. Bt: biotite, Chl: chlorite, Ms: muscovite. Reference data: Sheppard (1986); Ohmoto (1986).

5.3. *Fluid evolution and ore deposition*

Three different fluids were identified:

- Type I is a high-temperature (288–442 °C) and moderate salinity (8.8–13.7 wt% NaCl eq.), H_2O-NaCl aqueous fluid, related to the main W-Sn ore stage (stage II). This fluid probably derived from a magmatic source, since its salinity is in the range of bulk magmatic fluids (5–15 wt% NaCl eq.) for pressures between 1 and 2 kbar and temperatures between 700 and 400 °C (Audétat, 2019). The $\delta^{18}O$–δD isotope data support this hypothesis (Fig. 20). This fluid corresponds to the stage II of mineralization, related to the main W-Sn mineralization in quartz veins.
- Type II is a high-temperature (262–339 °C) and low salinity aqueous-carbonic H_2O-CO_2-N_2-CH_4-NaCl fluid (1.9–7.3 wt% NaCl eq.). This fluid corresponds to the third stage of mineralization, related to deposition of sulfides.
- Type III is an aqueous (H_2O-NaCl) fluid, trapped in secondary fluid inclusions. Therefore, it will not be used to discuss the evolution of the hydrothermal system.

In Peña do Seo, W and Sn mineralization in veins is linked to a H_2O-NaCl fluid, as only aqueous, carbonic-free inclusions have been found in W-Sn bearing veins (stage II). Temperature, salinity and the $\delta^{18}O$–δD isotopic signature allow interpreting a magmatic origin for this fluid. Ore fluids with similar characteristics have been identified in other W-Sn deposits worldwide, as in Germany (Korges et al., 2017) and China (Hu et al., 2012; Ni et al., 2015; Legros et al., 2019), but are uncommon in deposits in Iberia, where W deposition is generally related to metamorphic fluids with CO_2-CH_4-N_2 volatile components (Noronha et al., 1999; Mangas and Arribas, 1988b; Chicharro et al., 2016). A decrease in salinity together with a limited decrease of temperature occurred as the fluid evolved from Type I (stage II) to Type II (stage III), indicating that dilution could have led to deposition of sulfides in stage III, besides other mechanisms.

CO_2 in the Type II fluid might have been formed through fluid-rock interaction by decarbonation of wallrocks (Lowestern, 2001), but the absence of carbonates close to the quartz veins rather suggests it must have formed as a result of oxidation of CH_4, as previously suggested by Fuertes-Fuente et al. (2000). The origin of CH_4 is probably in the organic matter present in the host metasedimentary sequences, via CO_2 reduction (Roedder, 1984, Dubessy et al., 1989, Wilkinson, 1990; Cepedal et al., 2013, Tittel et al., 2019). No participation of meteoric fluids has been found. Sulfide mineralization in stage III is most probably related to interaction between the magmatic-hydrothermal fluid (Type I) and the host quartz schists.

Temperature-pressure conditions for the different mineralizing stages and temperature limits for the different fields have been reconstructed using fluid inclusion isochores (Fig. 21). Type I fluid circulated at temperatures between 280 and 450 °C and pressures between 60 and 330 MPa, which are quite common conditions for Sn-W deposits in Spain (e.g., Chicharro et al., 2016). Evidence of boiling was not found, which may be explained due to high pressures preventing this process. This accords well with the intermediate fluid density and moderate salinity calculated for type I fluid inclusions. Type II fluid circulated at lower temperatures, between 260 °C and 340 °C, and pressures between 160 and 310 MPa. The $\delta^{18}O$–δD values of the fluids in equilibrium with minerals from this stage (Ms, Chl), which plot in the metamorphic water field (Fig. 20), indicate participation of either fluids derived from the metasedimentary host rocks or magmatic fluids that interacted and partially equilibrated isotopically with the host metamorphic rocks (Harlaux et al., 2021a).

In Peña do Seo, tin and tungsten were deposited at temperatures between 435 °C and 270 °C. This is in agreement with Naumov et al. (2011), which concluded that the optimum temperature range for cassiterite precipitation is 450–300 °C, and 350–240 °C for wolframite; also, with Wood and Samson (2000), who reported 200–500 °C and 200–1500 bars as the most favorable P-T ranges for wolframite deposition. Sulfides were deposited in quartz veins at lower temperatures in the range between 340 and 260 °C. Abundant chlorite is found in veins containing aquocarbonic inclusions, indicating low-grade contact metamorphism conditions. CO_2 is the main constituent of the volatile phase, whereas N_2 and CH_4 are found in small amounts. N_2 probably derived from the minerals containing ammonium (NH_4^+), mainly feldspars and micas (Wang et al., 2018).

Thermal metamorphism (in addition to fluid circulation and mobilization) could have partly dehydrated muscovite, a mineral phase that can have relatively elevated contents of W (Michaud et al., 2021; Zhao et al., 2021). This would lead to W liberation to the fluids and ultimately, to the W mineralization. Additional elements (Fe and Mn) are needed for

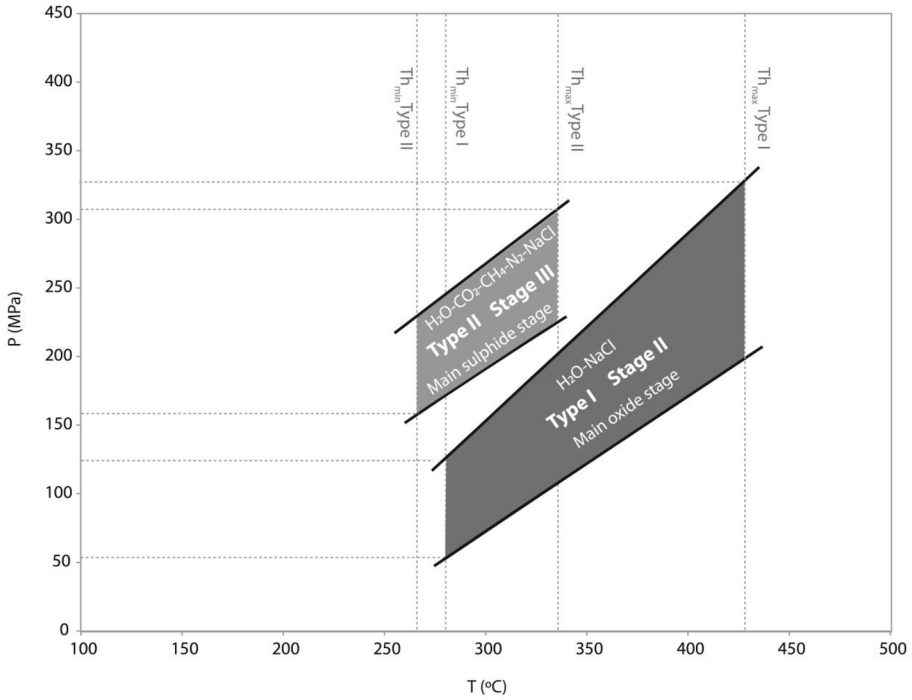

Fig. 21. Pressure–temperature reconstruction of fluids involved in the mineralization at the Peña do Seo deposit. Data from homogenization temperature (Th) of fluid inclusions.

wolframite deposition. The source of these elements is still highly debated. Heinrich (1990) proposes that they are mostly transported as complexes with Cl^-: $H_2WO_4 + (Fe,Mn)Cl_2 = (Fe,Mn)WO_4 + 2\ HCl$, whereas Lecumberri-Sánchez et al. (2017b) suggest that fluid-rock interaction is decisive, and Fe and Mn would be mainly leached from the host rocks into the veins. In Peña do Seo, Mn content in the schists is relatively high (532 ppm on average), and decreases in altered schists (371 ppm on average), indicating host quartz schists may have provided at least part the required Mn for wolframite deposition. Quartz schists may be the source of Fe for wolframite deposition as well given their high Fe_2O_3 contents (7.28 wt% on average).

The high abundance of F (and Sn) in the granitoid breccias (Table 1) indicates that fluorine could have been carried as fluoride-complexes (Barsukov, 1974; Štemprok, 1982). The enrichment of F in the residual melt reduces the tendency of Cl to partition into the fluid, thus making latest exsolving fluids more prone to transport W, and less to transport Sn (Audétat et al., 2000). Wolframite mineralization only appears in veins, whereas cassiterite mineralization is mostly found in granitoid breccias. This different behavior of W and Sn may be explained by opposed fluid-melt partitioning of both elements, with a marked preference of W for fluid and of Sn for melt at P-T conditions of 750 °C and 200 MPa, respectively (Schmidt et al., 2020), which would explain why Sn content in the granitoid breccias (848 ppm on average) is much higher than W content (24.5 ppm on average). Nevertheless, the elevated Sn content of the granitoid breccias could also be explained by the dehydration melting of biotite, as previously indicated (chapter 5.1, op. cit.).

As for the mechanisms involved in W and/or Sn deposition, fluid mixing is the most common in W-Sn deposits worldwide. In the case of Peña do Seo, we have not found evidence of mixing with meteoric waters in the ore system, but we cannot exclude the potential role of mixing between magmatic and metamorphic waters, or the rapid decompression induced by hydrofracturing of the host metamorphic rocks. Thus, mechanisms responsible for precipitation of wolframite and cassiterite are still not fully determined, although several processes (fluid-rock interaction, mixing, decompression, cooling) could have caused the precipitation of ore minerals.

6. Conclusions

Three main phases of mineralization related to at least two types of fluids are found in the Peña do Seo W-Sn vein-type deposit:

I) The oxide-halide-sulfide stage led to cassiterite-pyrite-fluorite mineralization (with minor arsenopyrite and chalcopyrite) in granitoid breccias, related to magmatic-hydrothermal fluids.
II) Wolframite and cassiterite mineralization was related to aqueous (H_2O–NaCl) magmatic-hydrothermal fluids, in two substages: wolframite mineralization in selvages, and wolframite and minor cassiterite mineralization in quartz veins.
III) Sulfide mineralization was related to (H_2O–CO_2–CH_4–N_2–NaCl) fluids that would have either derived from the metasedimentary host rocks or resulted from the interaction between magmatic fluids with the host metamorphic rocks.

Several processes (fluid-rock interaction, fluid mixing, decompression, cooling) could have triggered tungsten and tin precipitation in veins during stage II. Fluid dilution observed in the evolution of fluids was likely the main mechanism driving the deposition of sulfides.

Tin and part of the W mineralization could have been related to the crystallizing magmas of the Cadafresnas granites and granitoid breccias. Another part of the W mineralization could have been derived from the country rock schists via contact metamorphism, partial dehydration reactions and fluid circulation. Host quartz schists would have supplied the required Fe and Mn for wolframite and sulfide precipitation. Manganese was probably carried in magmatic-hydrothermal fluids together with W and Sn.

Declaration of Competing Interest

The authors declare that they have no known competing financial interests or personal relationships that could have appeared to influence the work reported in this paper.

Data availability

Data will be made available on request.

Acknowledgements

This work was funded by Project 0284_ESMIMET_3_E (INTERREG V-A Spain-Portugal Cooperation Programme, 2014-20) and by Project LE167G18 (Junta de Castilla y León, Spain). Research of PC is funded by a PhD grant from the University of León (Spain). The authors are grateful to Matthieu Harlaux, Editor Lisard Torró and an anonymous reviewer for their constructive comments, which significantly improved the quality of the manuscript. The excellent editorial handling by Editor-in-Chief Franco Pirajno is also greatly appreciated.

References

Abril-Hurtado, J, Matte, P., Rodríguez-Fernández, L.R. (1981). Memoria de la Hoja n° 157 (Oencia). Mapa Geológico de España E 1:50.000. Segunda Serie (MAGNA), Primera Edición. IGME. 48 pp. Depósito Legal: M-15396-1981.

Arribas, A. Jr, Gonzalo, F.J., Iglesias, M. (1982b). Génesis de una mineralización asociada a una cúpula granítica: el yacimiento de estaño de Golpejas (Salamanca). Cadernos do Laboratorio Xeolóxico de Laxe: Revista de xeoloxía galega e do hercínico peninsular, N° 3, 563-594.

Arribas, A. Jr. (1982a). Geología y metalogenia del yacimiento "Virgen de La Encina", Ponferrada, León. BSc Thesis. Universidad de Salamanca, Salamanca (Spain).

Audétat, A., Günther, D., Heinrich, C.A. (1998). Formation of a magmatic-hydrothermal ore deposit: insights with LA-ICP-MS analysis of fluid inclusions. Science, 279(5359): 2091-2094. doi: 10.1126/science.279.5359.2091.

Audétat, A., Günther, D., Heinrich, C.A., 2000. Magmatic-hydrothermal evolution in a fractionating granite: a microchemical study of the Sn-W-F-mineralized Mole Granite (Australia). Geochim. Cosmochim. Acta 64 (19). https://doi.org/10.1016/s0016-7037(00)00428-2.

Audétat, A. The Metal Content of Magmatic-Hydrothermal Fluids and Its Relationship to Mineralization Potential (2019). Economic Geology, 114 (6): 1033–1056. doi: 10.5382/econgeo.4673.

Bakker, R.J., 1997. Clathrates: Computer programs to calculate fluid inclusion V-X properties using clathrate melting temperatures. Comput. Geosci. 23, 1–18. https://doi.org/10.1016/S0098-3004(96)00073-8.

Bakker, R.J., 1998. Improvements in clathrate modelling II: the H_2O-CO_2-CH_4-N_2-C_2H_6 fluid system. Geol. Soc. Lond. Spec. Publ. 137 (1), 75–105. https://doi.org/10.1144/GSL.SP.1998.137.01.06.

Bakker, R.J., 2003. Package FLUIDS 1. Computer programs for analysis of fluid inclusion data and for modelling bulk fluid properties. Chem. Geol. 194, 3–23. https://doi.org/10.1016/S0009-2541(02)00268-1.

Bakker R.J., Brown, P.E. (2003). Computer modelling in fluid inclusion research. In: Fluid Inclusions, Analysis and Interpretation (eds. Samson I, Anderson A, Marshall D), Short Course v. 32, Mineralogical Association of Canada, pp. 175-212.

Bakker, R.J., Boiron M.C, Thiéry, R., Dubessy J., Cathelineau, M. (1996). Computerised clathrate stability model: specification of metamorphic fluids in inclusions. V.M. Goldschmidt Conference (Abstracts), v. 1, p. 37.

Bakker, R. J. (1999). Adaptation of the Bowers and Helgeson (1983) equation of state to the H_2O–CO_2–CH_4–N_2–NaCl system. Chemical Geology, Volume 154, Issues 1–4, pp. 225-236, ISSN 0009-2541. doi: 10.1016/S0009-2541(98)00133-8.

Ballouard, C., Poujol, M., Boulvais, P., Branquet, Y., Tartèse, R., and Vigneresse, J.L. (2016). Nb-Ta fractionation in peraluminous granites: A marker of the magmatic-hydrothermal transition. Geology, v. 44, p. 231–234. doi: 10.1130 /G37475.1.

Barsukov V.L. (1974) — Basic geochemical features of tin. Moscow, Nauka, 148 pp. (in Russian).

Bea, F., 1996. Residence of REE, Y, Th and U in granites and crustal protholiths; implications for the chemistry of crustal melts. J. Petrol. 37 (3), 521–552.

Bergström, S., 2020. Fluid inclusions and geochemistry of the Peña del Seo W-deposit, northwest Spain : Controlling mechanisms for tungsten deposition (MsC dissertation). Luleå University of Technology, Sweden.

Bodnar, R.J., 1993. Revised equation and table for determining the freezing point depression of H_2O-NaCl solutions. Geochim. Cosmochim. Acta 57, 683–684. https://doi.org/10.1016/0016-7037(93)90378-A.

Borthwick, J., Harmon, R.S.A., 1982. Note regarding ClF_3 as an alternative to Br $_F$5 for oxygen isotope analysis. Geochim. Cosmochim. Acta 46, 1665–1668. https://doi.org/10.1016/0016-7037(82)90321-0.

Bowers, T.S., Helgeson, H.C., 1983. Calculation of the thermodynamic and geochemical consequences of nonideal mixing in the system H_2O–CO_2–NaCl on phase relations in geological systems: equation of state for H_2O–CO_2–NaCl fluids at high pressures and temperatures. Geochim. Cosmochim. Acta 47, 1247–1275. https://doi.org/10.1016/0016-7037(83)90066-2.

Brown, M., Korhonen, F.J., 2009. Some remarks on melting and extreme metamorphism of crustal rocks. In: Gupta, A.K., Dasgupta, S. (Eds.), Physics and chemistry of the earth's interior. Springer, New Delhi, pp. 67–88.

Burkhardt, R., García, A., 1985. Distribución de Au y Ag en filones de cuarzo mineralizados (W, Sn, sulfuros) del Oeste de España. Cuad. Lab. Xeol. Laxe 10, 285–310.

Capdevila, R., Floor, P. (1970). Les différents types de granites hercyniens et leur distribution dans le nord ouest de l'Espagne: Boletín Geológico y Minero, v. LXXXI, p. 215–225.

Capdevila, R. (1969). Le metamorphisme regional progressif et les granites dans le segment Hercynien de Galice Nord Orientale (NW de L'Espagne) [Ph.D. thesis]: Montpellier, France, Université de Montpellier, 430 p.

Cepedal, A., Fuertes-Fuente, M., Martín-Izard, A., García-Nieto, J., Boiron, M.C., 2013. An intrusion-related gold deposit (IRGD) in the NW of Spain, the Linares deposit: igneous rocks, veins and related alterations, ore features and fluids involved. J. Geochem. Explor. 124, 101–126. https://doi.org/10.1016/j.gexplo.2012.08.010.

Chappell, B.W., White, A.J., 2001. Two contrasting granite types: 25 years later. Aust. J. Earth Sci. 48 (4), 489–499.

Chicharro, E., Martín-Crespo, T., Gómez-Ortiz, D., López-García, J.Á., Oyarzun, R., Villaseca, C., 2015. Geology and gravity modeling of the Logrosán Sn–(W) ore deposits (Central Iberian Zone, Spain). Ore Geol. Rev. 65, 294–307. https://doi.org/10.1016/j. oregeorev.2014.10.005.

Chicharro, E., Boiron, M.C., López-García, J.A., Barfod, D.N., 2016. Origin, ore forming fluid evolution and timing of the Logrosán Sn-(W) ore deposits (Central Iberian zone, Spain). Ore Geol. Rev. 72, 896–913. https://doi.org/10.1016/j.oregeorev.2015.09.020.

Chicharro, E. (2010). Caracterización geológica de las mineralizaciones de Sn-(W) asociadas al stock granítico de Logrosán (Cáceres). Proyectos de Máster (UCM), 54 pp.

Clarke, D.B., Renno, A.D., Hamilton, D.C., Gilbricht, S., Bachmann, K., 2021. The spatial association of accesory minerals with biotite in granitic rocks from the South Mountain batholith, Nova Scotia, Canada. Geosphere 18 (1), 1–18.

Claypool, G.E., Holser, W.T., Kaplan, I.R., Sakai, H., Zak, I., 1980. The age curves of sulfur and oxygen isotopes in marine sulfate and their mutual interpretation. Chem. Geol. 28, 199–260. https://doi.org/10.1016/0009-2541(80)90047-9.

Clayton, R.N., Mayeda, T.K., 1963. The use of bromine pentafluoride in the extraction of oxygen from oxides and silicates for isotopic analysis. Geochim. Cosmochim. Acta 27, 43–52. https://doi.org/10.1016/0016-7037(63)90071-1.

Clayton, R.N., O'Neil, J.R., Mayeda, T.K., 1972. Oxygen isotope exchange between quartz and water. J. Geophys. Res. 77 (17), 3057–3067. https://doi.org/10.1029/JB077i017p03057.

Clemens, J., Stevens, G., 2012. What controls chemical variation in granitic magmas? Lithos 134–135, 317–329. https://doi.org/10.1016/j.lithos.2012.01.001.

Corretgé, L.G., Suárez, O., Galán, G., Fernández-Suárez. (2004). Magmatismo (en: 2.3. Zona Asturoccidental-Leonesa). In: Vera, J.A. (Ed.), Geología de España. SGE-IGME. Madrid, pp. 63-68.

Cotelo-Neiva, J.M. (1944). Jazigos portugueses de cassiterite e de volframite. Comunicações dos Serviços Geológicos de Portugal, Tomo XXV: 251pp.

Cuesta, A., Gallastegui, G. (2004). Magmatismo de la Zona Centroibérica: Galicia occidental. In: Vera, J.A. (ed.). Geología de España. Sociedad Geológica de España – Instituto Geológico y Minero de España (SGE-IGME), Madrid, 96-100.

Deicha, G., (1973). Microfissuration du quartz granitique et circulation des fluids géochimiques d'origine plutonique. Coll. "Raguin", 8 méthodes d'études. Masson, Paris.

Duan, Z., Møller, N., Weare, J.H., 1996. A general equation of state for supercritical fluid mixtures and molecular dynamics simulation of mixture PVTX properties. Geochim. Cosmochim. Acta 60, 1209–1216.

Dubessy, J., 1984. Simulation des équilibres chimiques dans le système C-O-H. Conséquences méthodologiques pour les inclusions fluides. Bull. Minéral. 107, 155–168. https://doi.org/10.3406/bulmi.1984.7746.

Dubessy, J., Poty, B., Ramboz, C., 1989. Advances in C-O-H-N-S fluid geochemistry based on micro-Raman spectrometry analysis of fluid inclusions. Eur. J. Mineral. 1, 517–534. https://doi.org/10.1127/ejm/1/4/0517.

Dubessy, J., Thiéry, R., Canals, M., 1992. Modelling of phase equilibria involving mixed gas clathrates: application to the determination of molar volume of the vapour phase and salinity of aqueous solution in fluid inclusions. Eur. J. Mineral 4 (5), 873–884. https://doi.org/10.1127/ejm/4/5/0873.

European Comission (2011). COMMUNICATION FROM THE COMMISSION TO THE EUROPEAN PARLIAMENT, THE COUNCIL, THE EUROPEAN ECONOMIC AND SOCIAL COMMITTEE AND THE COMMITTEE OF THE REGIONS. Tackling the Challenges in Commodity Markets and on Raw Materials. COM/2011/0025 final. Brussels.

European Comission (2020a) COMMUNICATION FROM THE COMMISSION TO THE EUROPEAN PARLIAMENT, THE COUNCIL, THE EUROPEAN ECONOMIC AND SOCIAL COMMITTEE AND THE COMMITTEE OF THE REGIONS. Critical Raw Materials Resilience: Charting a Path towards greater Security and Sustainability. COM/2020/474 final. Brussels.

European Commission (2020b). Study on the EU's list of Critical Raw Materials – Final Report.

European Commission (2020c). Study on the EU's list of Critical Raw Materials, Factsheets on Non-critical Raw Materials.

Fernández-Fernández, A., Prieto, R., Timón-Sánchez, S., Moro-Benito, M. C. (2019). Indicios de oro en el Distrito Minero de Calabor: Área de Hermisende-La Tejera (Zamora). Macla: revista de la Sociedad Española de Mineralogía, (24), 20.

Fernández-Suárez, J., Dunning, G., Jenner, G.A., Gutierrez-Alonso, G., 2000. Variscan collisional magmatism and deformation in NW Iberia: Constraints from U-Pb geochronology of granitoids. J. Geol. Soc. London 157, 565–576. https://doi.org/10.1144/jgs.157.3.565.

Fernández-Suárez, J. (1994). Petrología de los granitos peralumínicos y metamorfismo de la banda Boal-Los Ancares. PhD thesis, Departamento de Geología, Univ. de Oviedo, 1-418.

Fuertes-Fuente, M., Martín-Izard, A., Boiron, M.C., Viñuela, J.M., 2000. P-T path and fluid evolution in the Franqueira granitic pegmatite, central Galicia, northwestern Spain. Can. Mineral. 38, 1163–1175. https://doi.org/10.2113/gscanmin.38.5.1163.

Fuertes-Fuente, M., Cepedal, A., Lima, A., Dória, A., Ribeiro, M.A., Guedes, A., 2016. The Au-bearing vein system of the Limarinho deposit (northern Portugal): Genetic constraints from Bi-chalcogenides and Bi–Pb–Ag sulfosalts, fluid inclusions and stable isotopes. Ore Geol. Rev. 72, 213–231.

Godfrey, J.D., 1962. The deuterium content of hydrous minerals from the east-central Sierra Nevada and Yosemite National Park. Geochim. Cosmochim. Acta 26, 1215–1245. https://doi.org/10.1016/0016-7037(62)90053-4.

Gómez-Fernández, F., Vindel, E., Martín-Crespo, T., Sánchez, V., González Clavijo, E., Matías, R., 2012. The Llamas de Cabrera gold district, a new discovery in the Variscan basement of northwest Spain: a fluid inclusion and stable isotope study. Ore Geol. Rev. 46, 68–82. https://doi.org/10.1016/j.oregeorev.2012.02.001.

Gómez-Fernández, F., Cunningham, J.K., Caldevilla, P., Herrero-Hernández, A., Beard, A. D., 2021. Microscopic and NanoSIMS characterization of black shale-hosted pre-kinematic pyrites: possible gold source of the orogenic gold deposits in the Truchas Syncline (Variscan Iberian Massif). Ore Geol. Rev. 138, 104344 https://doi.org/10.1016/j.oregeorev.2021.104344.

Gonçalves, A., Lima, L., Mota, A., Ramos, V., Barros, J., Noronha, F., 2017. The Santa Helena Breccia Pipe (Borralha – North Portugal). A new type of W ore deposit in the Iberian Tin-Tungsten metallogenic province. Comunicaçoes Geologicas 104, 55–60.

González-Menéndez, L., Gallastegui, G., Cuesta, A., González Cuadra, P., Rubio-Ordóñez, A. (2019). Granitos y rocas metamórficas del Oeste de Galicia (costa occidental gallega - Isla de Ons). 6ª Reunión del Grupo Ibérico de Petrología, Geoquímica y Geocronología. Sociedad Geológica de España. 92 pp.

Gonzalo, F.J., García, A.S., 1984. Yacimientos de estaño del oeste de España. Ensayo de caracterización y clasificación económicas. Cuad. Lab. Xeol. Laxe. 9, 265–294.

Hannah, J.L, Stein, H.J. (1990). "Magmatic and hydrothermal processes in ore-bearing systems", in Stein, H.J., Hannah, J.L., eds., Ore-bearing granite systems; Petrogenesis and mineralizing processes: Geological Society of America Special Paper 246. doi: 10.1130/SPE246-p1.

Harlaux, M., Mercadier, J., Marignac, C., Peiffert, C., Cloquet, C., and Cuney, M. (2018b). Tracing metal sources in peribatholitic hydrothermal W deposits based on the chemical composition of wolframite: The example of the Variscan French Massif Central: Chemical Geology, v. 479, p. 58-85.

Harlaux, M., Marignac, C., Mercadier, J., Poujol, M., Boiron, M.C., Kouzmanov, K., Camacho, A., Alikouss, S., Roméo, B., Mouthier, B., and Cuney, M. (2021a) Multistage development of a hydrothermal W deposit during the Variscan late-orogenic evolution: the Puy-les-Vignes breccia pipe (Massif Central, France): BSGF-Earth Sciences Bulletin, v. 192, p. 33.

Harlaux, M., Romer, R.L., Mercadier, J., Morlot, C., Marignac, C., Cuney, M., 2018a. 40 Ma of hydrothermal W mineralization during the Variscan orogenic evolution of the French Massif Central revealed by U-Pb dating of wolframite. Miner. Deposita 53, 21–51.

Harlaux, M., Kouzmanov, K., Gialli, S., Marger, K., Bouvier, A.S., Baumgartner, L.P., Rielli, A., Dini, A., Chauvet, A., Kalinaj, M., Fontboté, L., 2021. Fluid mixing as primary trigger for cassiterite deposition: evidence from in situ δ18O-δ11B analysis of tourmaline from the world-class San Rafael tin (-copper) deposit, Peru. Earth and Planetary Science Letters 563, 116889. https://doi.org/10.1016/j.epsl.2021.116889.

Heinrich, C.A., 1990. The chemistry of hydrothermal tin(-tungsten)ore deposition. Econ. Geol. 85, 457–481. https://doi.org/10.2113/gsecongeo.85.3.457.

Heinrich, C.A., 2007. Fluid-fluid interactions in magmatic-hydrothermal ore formation. Rev. Mineral. Geochem. 65 (1), 363–387. https://doi.org/10.2138/rmg.2007.65.11.

Hoefs, J., 2009. Isotope fractionation processes of selected elements. In: Stable Isotope Geochemistry. Springer, Berlin, Heidelberg. https://doi.org/10.1007/978-3-540-70708-0_2.

Hoefs, J., Emmermann, R., 1983. The oxygen isotope composition of Hercynian granites and pre-Hercynian gneisses from the Schwarzwald, S.W. Germany. Contrib. Mineral. Petrol. 83, 320–329. https://doi.org/10.1007/BF00371200.

Ishikawa, Y., Sawaguchi, T., Iwaya, S., Horiuchi, M., 1976. Delineation of prospecting targets for Kuroko deposits based on modes of volcanisms of underlying dacite and alteration haloes (in Japanese). Mining Geology 26, 105–117. https://doi.org/10.11456/shigenchishitsu1951.26.105.

Jackson, N.J., Halliday, A.N., Sheppard, S.M.F., Mitchell, J.G., 1982. Hydrothermal activity inthe St. Just mining district, Cornwall, England. In: Evans, M. (Ed.), Metallization Associated With Acid Magmatism Chichester. Wiley, pp. 137–179.

Jackson, N.J., Willis-Richards, J., Manning, D.A., Sams, M.S., 1989. Evolution of the Cornubian ore field, Southwest England; Part II, Mineral deposits and ore-forming processes. Econ. Geol. 84, 1101–1133.

Jenkin, G.R.T., 1988. Stable isotope studies in Caledonides of SW Connemara, Ireland. Univ. Glasgow, UK. PhD thesis.

Julivert, M., Fontboté, J.M., Ribeiro, A. and Conde, L. (1972). Mapa Tectónico de la Península Ibérica y Baleares E. 1:1.000.000. Inst. Geol. Min. España, Madrid, 113 p.

Junta de Castilla y León (1986). Estudio geológico-minero de la zona de Hermisende (Prov. de Zamora). Informe interno, 21.

Kelly, W.C., Rye, R.O., 1979. Geologic, fluid inclusion, and stable isotope studies of the tin-tungsten deposits of Panasqueira, Portugal. Econ. Geol. 74 (8), 1721–1822. https://doi.org/10.2113/gsecongeo.74.8.1721.

Korges, M., Weis, P., Lüders, V., Laurent, O., 2017. Depressurization and boiling of a single magmatic fluid as a mechanism for tin-tungsten deposit formation. Geology 46 (1), 75–78. https://doi.org/10.1130/g39601.1.

Kronsell, I. (2019). Structural control on the Peña del Seo tungsten-greisen vein deposit, northwest Spain. (MsC dissertation). Luleå University of Technology, Sweden.

Large, R.R., Gemmell, J.B., Paulick, H., Huston, D.L., 2001. The alteration box plot: a simple approach to understanding the relationship between alteration mineralogy and lithogeochemistry associated with volcanic-hosted massive sulfide deposits. Econ. Geol. 96 (5), 957–971. https://doi.org/10.2113/gsecongeo.96.5.957.

Lecumberri-Sánchez, P., Vieira, R., Heinrich, C.A., Pinto, F., Wälle, M. (2017b). Geology, 45, (7), 579–582. Fluid-rock interaction is decisive for the formation of tungsten deposits. doi: 10.1130/G38974.1.

Lecumberri-Sánchez, P., Heinrich, C. A., Wälle, M., Codeço, M. S., Weis, P., Pinto, F., Vieira, R. (2017a). Fluid Sources at the Panasqueira Tungsten-Vein Deposit - Abstracts, AGU 2017 Fall Meeting (New Orleans, USA 2017).

Legros, H., Richard, A., Tarantola, A., Kouzmanov, K., Mercadier, J., Vennemann, T., Marignac, C., Cuney, M., Wang, R.C., Charles, N., Bailly, L., Lespinasse, M.Y., 2019. Multiple fluids involved in granite-related W-Sn deposits from the world-class Jiangxi province (China). Chemical Geology, Elsevier 508, 92–115. https://doi.org/10.1016/j.chemgeo.2018.11.021.

Lehmann, B., 2021. Formation of tin ore deposits: a reassessment. Lithos 402–403, 105756. https://doi.org/10.1016/j.lithos.2020.105756.

Liu, X., Ma, Y., Xing, H., Zhang, D., 2018. Chemical responses to hydraulic fracturing and wolframite precipitation in the vein-type tungsten deposits of southern China. Ore Geol. Rev. https://doi.org/10.1016/j.oregeorev.2018.08.027.

Llorens, T., Moro, M. C. (2012a). Oxide minerals in the granitic cupola of the Jálama Batholith, Salamanca, Spain. Part II: Sn, W and Ti minerals in intra-granitic quartz veins. Journal of Geosciences, volume 57, issue 3, 155 - 171. doi: 10.3190/jgeosci.119.

Llorens, T., Moro, M.C., 2012. Fe-Mn phosphate associations as indicators of the magmatic-hydrothermal and supergene evolution of the Jálama Batholith in the Navasfrías Sn-W District, Salamanca, Spain. Mineral Mag. 76, 1–24. https://doi.org/10.1180/minmag.2012.076.1.1.

Llorens, T. (2011). The Sn-W-(Nb-Ta) Magmatic-Hydrothermal Mineralizations of the Navasfrías District (SW Salamanca). Ph.D. thesis, Salamanca University. 290: pp 1-353. ISBN 978-84-7800-088-3.

Mangas, J., Arribas, A., 1988a. Evolution of hydrothermal fluids in the Feli tin deposit, western Spain. Bull. Minéral. 111, 343–358. https://doi.org/10.3406/bulmi.1988.8057.

Mangas, J., Arribas, A., 1988b. Hydrothermal fluid evolution of the Sn-W mineralization in the Parrilla ore deposits (Cáceres, Spain). J. Geol. Soc. London 145, 147–153. https://doi.org/10.1144/gsjgs.145.1.0147.

Marignac, C., Cuney, M., 1999. Ore deposits of the French Massif Central: insight into the metallogenesis of the Variscan collision belt. Mineral. Deposita 34, 472–504. https://doi.org/10.1007/s001260050216.

Martínez, F.J., Suárez, O., Corretgé, L.G. (2004). Características generales del metamorfismo sinorogénico (Zona Asturoccidental-Leonesa). In: Geología de España, J.A. Vera, Ed. Chp: 2.3.2.3., 55-58.

Martínez-Abad, I., Cepedal, A., Arias, D., Martin-Izard, A., 2015. The Vilalba gold district, a new discovery in the Variscan terranes of the NW of Spain: a geologic, fluid inclusion and stable isotope study. Ore Geol. Rev. 66, 344–365. https://doi.org/10.1016/j.oregeorev.2014.10.021.

Martinez-Catalán, J.R., Perez Estaun, A., Bastida, F., Pulgar, J.A., Marcos, A. (1990). Structure. In: Dallmeyer, R.D., Garcia, E.M. (eds) Pre-Mesozoic Geology of Iberia. IGCP-Project 233. Springer, Berlin, Heidelberg. doi: 10.1007/978-3-642-83980-1_9.

Martínez-Catalán, J.R., Arenas, R., Díaz-García, F., Gómez-Barreiro, J., González-Cuadra, P., Abati, J., Castiñeiras, P., Fernández-Suárez, J., Sánchez-Martínez, S., Andonaegui, P., Gónzalez-Clavijo, E., Díez-Montes, A., Rubio-Pascual, F.J. Valle-Aguado, B. (2007). Space and time in the tectonic evolution of the northwestern Iberian Massif. Implications for the comprehension of the Variscan belt. In: Hatcher, R.D., Jr., Carlson, M.P., McBride, J.H., Martínez Catalán, J.R. (Eds.), 4-D framework of continental crust. Geological Society of America Memoir.

Martínez-Catalán, J.R., Aller, J.; Alonso, J.L.; Bastida, F. (2009). The Iberian Variscan orogen. In A. García-Cortés (Ed.). Spanish geological frameworks and geosites: an approach to Spanish geological heritage of international relevance. Publications of the Geological Survey of Spain.

Matte, P., 1968. Précisions sur le Precambrien supèrieur schistogrèseux de l'ouest des Asturies. Comparison aver les autres affleurements precambrien du nordouest de l'Espagne. Revue Géogr. Phys. Géol. Dyn. 10, 205–211.

McDonough, W.F., Sun, S.S., 1995. The composition of the Earth. Chem. Geol. 120, 223–253.

Michaud, J.-A.-S., Pichavant, M., Villaros, A., 2021. Rare elements enrichment in crustal peraluminous magmas: insights from partial melting experiments. Contrib. Miner. Petrol. 176, 96.

Monnier, L., Salvi, S., Melleton, J., Bailly, L., Béziat, D., de Parseval, P., Gouy, S., Lach, P., 2019. Multiple generations of wolframite mineralization in the Echassieres District (Massif Central, France). Minerals 9, 637. https://doi.org/10.3390/min9100637.

Moura, A., Dória, A., Neiva, A.M.R., Leal-Gomes, C., Creaser, R.A., 2014. Metallogenesis at the Carris W-Mo–Sn deposit (Gerês, Portugal): constraints from fluid inclusions, mineral geochemistry, Re–Os and He–Ar isotopes. Ore Geol. Rev. 56, 73–93. https://doi.org/10.1016/j.oregeorev.2013.08.001.

Naumov, V.B., Dorofeev, V.A., Mironova, O.F., 2011. Physicochemical parameters of the formation of hydrothermal deposits: a fluid inclusion study. I. Tin and tungsten deposits. Geochem. Int. 49, 1002. https://doi.org/10.1134/S0016702911100041.

Ni, P., Wang, X.D., Wang, G.G., Huang, J.B., Pan, J.Y., Wang, T.G., 2015. An infrared microthermometric study of fluid inclusions in coexisting quartz and wolframite from late Mesozoic tungsten deposits in the Gannan metallogenic belt, South China. Ore Geol. Rev. 65, 1062–1077. https://doi.org/10.1016/j.oregeorev.2014.08.007.

Noronha, F., 2017. Fluids and Variscan metallogenesis in granite related systems in Portugal-. Procedia Earth Planet. Sci. 17, 1–4. https://doi.org/10.1016/j.proeps.2016.12.002.
Noronha, F., Doria, A., Dubessy, J., 1992. Characterization and timing of the different types of fluids present in the barren and ore-veins of the W-Sn deposit of Panasqueira, Central Portugal. Miner. Deposita 27 (1992), 72–79. https://doi.org/10.1007/BF00196084.
Noronha, F., Vindel Catena, E., López García, J.Á., Dória, A., García García, E., Boiron, M.C., Cathelineau, M., 1999. Fluids related to tungsten ore deposits in northern Portugal and Spanish central system: a comparative study. Rev. Soc. Geol. Esp. 12, 397–403.
Noronha, F. (1983). Estudo metalogenético da área tungstífera da Borralha. PhD Thesis, Faculdade de Ciências da Universidade do Porto. Porto.
Ohmoto, H., 1986. Stable isotope geochemistry of ore deposits. Rev. Mineral. Geochem. 16, 491–559.
Pattison, D.R.M., De Capitani, C., Gaides, F., 2011. Petrological consequences of variations in metamorphic reaction affinity. J. Metam. Geol. 29, 953–977.
Pellitero, E., 1981a. La Zona volframífera centro-oriental de Salamanca. Cuadernos Laboratorio Xeolóxico de Laxe 2, 227–244.
Pellitero, E. (1981b). Factores geológicos y genéticos' de los yacimientos volframíferos del norte de la provincia de Salmanca. Cuadernos Laboratorió Xeolóxico de Laxe. Vol. 2, p. 245-258.
Pérez-Estaún, A.; Bea, F.; Bastida, F.; Marcos, A.; Martínez-Catalán, J.R.; Martínez-Poyatos, D.; Arenas, R.; Díaz-García, F.; Azor, A.; Simancas, J.F.; Gónzalez-Lodeiro, F. (2004). La Cordillera Varisca Europea: El Macizo Ibérico. In: Geología de España (J. Vera, ed.). SGE-IGME, Madrid, Spain, pp 21-25.
Polya, D.A., 1988. Efficiency of hydrothermal ore formation and the Panasqueira W-Cu (Ag)–Sn vein deposit. Nature 333 (6176), 838. https://doi.org/10.1038/333838a0.
Polya, D.A., 1989. Chemistry of the main-stage ore-forming fluids of the Panasqueira W-Cu (Ag)-Sn deposit, Portugal; implications for models of ore genesis. Econ. Geol. 84 (5), 1134–1152. https://doi.org/10.2113/gsecongeo.84.5.1134.
Prieto, A.C., Guedes, A., Dória, A., Noronha, F., Jiménez, J., 2012. Quantitative determination of gaseous phase compositions in fluid inclusions by Raman microspectrometry. Spectroscopy Lett.: Int. J. Rapid Commun. 45 (2), 156–160. https://doi.org/10.1080/00387010.2011.628737.
Robinson, W., Kusakabe, M., 1975. Quantitative preparation of sulfur dioxide, for 34S/32S analyses, from sulfides by combustion with cuprous oxide. Anal. Chem. 47, 1179–1181. https://doi.org/10.1021/ac60357a026.
Rodríguez Fernández, L.R., Toyos, J.M., Díez Montes, A., González Menéndez, L., Gallastegui, G., Heredia, N., Martín Parra, L.M., Rubio Pascual, F.J., Fernández Lozano, J. Castaño de Luis, R. (2021). Memoria de la Hoja n° 18 (Ponferrada). Mapa Geológico de España, E. 1:200.000. IGME, CSIC. Madrid. 129 p.
Roedder, E., 1984. Fluid Inclusions, Reviews in Mineralogy, 12. Mineralogical Society of America, Michigan.
Schmidt, C., Romer, R.L., Wohlgemuth-Ueberwasser, C.C., Appelt, O., 2020. Partitioning of Sn and W between granitic melt and aqueous fluid. Ore Geol. Rev. 117, 103263 https://doi.org/10.1016/j.oregeorev.2019.103263.
Seltmann, R., Štemprok, M., 1994. Textural evidence for the existence of two-phase granites in the Younger Intrusive Complex granites of the Krušné Hory/Erzgebirge province. J. Czech Geol. Soc. 39, 103–104.
Sharp, Z.D., 1990. A laser-based microanalytical method for the insitu determination of oxygen isotope ratios of silicates and oxides. Geochim. Cosmochim. Acta 54, 1353–1357. https://doi.org/10.1016/0016-7037(90)90160-M.
Shepherd, T.J., Rankin, A.H., Alderton, D.H.M., 1985. A Practical Guide to Fluid Inclusion Studies. Glasgow and London (Blackie), p. 239 pp..
Sheppard, S.M.F., 1986. Characterization and isotopic variations in natural water. Rev. Mineral. 16, 165–183.
Spear, F.S. (1993). Metamorphic Phase Equilibria and Pressure-Temperature-Time Paths. Mineralogical Society of America Monograph, 799 pp.
Štemprok, M., 1967. Genetische Probleme der Zinn-Wolfram-Vererzung im Erzgebirge. Mineral. Deposita 2, 102–118. https://doi.org/10.1007/BF00206583.
Štemprok, M. (1982). Tin-fluorine relationships in ore-bearing assemblages. In: Evans AM (ed) Metallization associated with acid magmatism, 6:321–337, John Wiley, New York.
Streckeisen, A., 1976. To each plutonic rock its proper name. Earth Sci. Rev. 12, 1–33.
Suárez, O., 1970. Estudio petrológico del plutón de Boal (Asturias, NW de España). Studia geologica salmanticensia 2, 93–113. ISSN 0211-8327.
Suzuoki, T., Epstein, S. (1976). Hydrogen isotope fractionation between OH-bearing minerals and water, Geochimica et Cosmochimica Acta, Volume 40, Issue 10, Pages 1229-1240,ISSN 0016-7037, doi: 10.1016/0016-7037(76)90158-7.
Sylvester, P.J., 1998. Post-collisional strongly peraluminous granites. Lithos 45, 29–44. https://doi.org/10.1016/S0024-4937(98)00024-3.
Tartèse, R., Boulvais, P., 2010. Differentiation of peraluminous leucogranites "en route" to the surface. Lithos 114, 353–368. https://doi.org/10.1016/j.lithos.2009.09.011.
Taylor, H.P., 1978. Oxygen and hydrogen isotope studies of plutonic granitic rocks. Earth Planet. Sci. Lett. 38 (1), 177–210. https://doi.org/10.1016/0012-821X(78)90131-0.
Thiéry, R., Van der Kerkhof, A.M., Dubessy, J., 1994. vX properties of CH4-CO2 and CO2-N2 fluid inclusions: modelling for T < 31 °C and P < 400 bars. Eur. J. Mineral. 6, 753–771.
Timón-Sánchez, S.M., Moro, M.C., Cembranos, M.L., 2009. Mineralogical and Physiochemical Evolution of the Los Santos Scheelite Skarn, Salamanca, NW Spain. Econ. Geol. 104, 961–995. https://doi.org/10.2113/econgeo.104.7.961.
Timón-Sánchez, S.M., Martínez Orio, R., Díez Montes, A., 2018. Óxidos de Sn-Ti-Nb-Ta en las venas de cuarzo de la Mina Arroyo del Valle Largo, Distrito de Morille-Martinamor (Salamanca). Macla 23, 89–90.
Tischendorf, G., Förster, H.-J., Gottesmann, B., 2001. Minor- and trace-element composition of trioctahedral micas: a review. Mineral. Mag. 65 (2), 249–276.
Tittel, J., Hüls, M., Koschorreck, M., 2019. Terrestrial vegetation drives methane production in the sediments of two German reservoirs. Sci. Rep. 9, 15944. https://doi.org/10.1038/s41598-019-52288-1.
Tornos, F., Casquet, T. (1984). La mineralización de W-Sn-Cu-Pb de Otero de Herreros (Segovia). Un skarn con una zona de cizalla superpuesta. I Congreso Español de Geología. Tomo U, p. 703-717.
Tornos, F., Galindo, C., Spiro, B.F. (2001). Isotope geochemistry of Los Santos (Spanish Central System) calcic scheelite skarn, constraints on the source of the fluids and tungsten, in Piestrzynski et al., eds., Mineral deposits at the beginning of the 21st century, p. 921–924.
US Department of the Interior. (2018). Final list of Critical Raw Materials. Federal Register / Vol. 83, No. 97, pp. 23295-23296 / Friday, May 18, 2018 / Notices.
Vallance, J., Cathelineau, M., Marignac, C., Boiron, M.-C., Fourcade, S., Martineau, F., Fabre, C., 2001. Microfracturing and fluid mixing in granites: W-(Sn) ore deposition at Vaulry (NW French Massif Central). Tectonophysics 336, 43–61. https://doi.org/10.1016/S0040-1951(01)00093-2.
Villaros, A., Stevens, G., Moyen, J.F., Buick, I.S., 2009. The trace element compositions of S-type granites: evidence for disequilibrium melting and accessory phase entrainment in the source. Contrib. Miner. Petrol. 158, 543–561.
Villaseca, C., Barbero, L., Villanueva, V., 1998. A re-examination of the typology of peraluminous granite types in intracontinental orogenic belts. Trans. R. Soc. Edinb. Earth Sci. 89 https://doi.org/10.1017/S0263593300007045.
Vindel, E., López-García, J.A., Boiron, M. C., Cathelineau, M., Prieto, A. C. (1995). P-V-T-X -f02 evolution from wolframite to sulfide depositional stages in intragranitic W-veins. An example from the Spanish Central System. Eur. J Mineral., 7, pp. 675-688. ISSN 0935-1221.
Wang, Y., Wang, K., Konare, Y., 2018. N2-rich fluid in the vein-type Yangjingou scheelite deposit, Yanbian, NE China. Sci. Rep. 8, 5662. https://doi.org/10.1038/s41598-018-22227-7.
Watson, E.B., Harrison, T.M., 1983. Zircon saturation revisited: temperature and composition effects in a variety of crustal magma types. Earth Planet. Sci. Lett. 64 (2), 295–304. https://doi.org/10.1016/0012-821x(83)90211-x.
Wei, W., Hu, R., Bi, X., Peng, J., Su, W., Song, S., Shi, S., 2012. Infrared microthermometric and stable isotopic study of fluid inclusions in wolframite at the Xihuashan tungsten deposit, Jiangxi province, China. Miner Deposita 47, 589–605. https://doi.org/10.1007/s00126-011-0377-0.
Whalen, J.B., Currie, K.L., Chapbell, B.W., 1987. A-type granites: geochemical characteristics, discrimination and petrogenesis. Contrib. Mineral. Petrol. 95, 407–419. https://doi.org/10.1007/BF00402202.
Wilkinson, J.J., 1990. The role of metamorphic fluids in the development of the Cornubian Orefield: fluid inclusion evidence from south Cornwall. Mineral. Mag. 54, 219–230. https://doi.org/10.1180/minmag.1990.054.375.08.
Witt, W.K., 1987. Fracture-controlled feldspathic alteration in granites associated with tin mineralization in the Irvinebank Emuford area, northeast Queensland. Australian J. Earth Sci. 34, 447–462. https://doi.org/10.1080/08120098708729425.
Wood, S.A., Samson, I.M., 2000. The hydrothermal geochemistry of tungsten in granitoid environments: I. Relative solubilities of ferberite and scheelite as a function of T, P, pH, and mNaCl. Econ. Geol. 95, 143–182.
Zamarreño, I., 1975. Peritidal origin of Cambrian carbonates in northwest Spain. In: Ginsburg, R.N. (Ed.), Tidal Deposits: A Case Book of Recent Examples and Fossil Countparts. Springer Verlag, Berlin Heidelberg, pp. 323–332. https://doi.org/10.1007/978-3-642-88494-8_33.
Zhang, Y.-G., Frantz, J.D., 1987. Determination of the homogenization temperatures and densities of supercritical fluids in the system NaCI-KCl-CaCl2-H20 using synthetic fluid inclusions. Chem. Geol. 64, 335–350. https://doi.org/10.1016/0009-2541(87)90012-X.
Zhao, P., Chu, X., Williams-Jones, A.E., Mao, J., Yuan, S., 2021. The role of phyllosilicate partial melting in segregating tungsten and tin deposits in W-Sn metallogenetic provinces. Geology 50 (1), 121–125.